Bulletin of Volcanology (2026) 88:51
https://doi.org/10.1007/s00445-026-01938-0

RESEARCH

Evidence of shallow storage and re-equilibration of magmas feeding the 39.8 ka Campanian Ignimbrite (Italy) eruption

Allyson N. Murray[1] · Michael H. Ort[1] · Kayla Iacovino[2] · Victoria C. Smith[3] · Guido Giordano[4] · Roberto Isaia[5]

Received: 20 October 2025 / Accepted: 11 January 2026

Abstract

The 39.8 ka Campanian Ignimbrite eruption from Campi Flegrei, Italy, emplaced voluminous Plinian fallout and deposits from dilute pyroclastic density currents. Elevated concentrations of magmatic volatiles have been proposed as a gas source for particle dilution of these pyroclastic density currents. Trace, major, and volatile element concentrations measured in 51 clinopyroxene-hosted melt inclusions from six Campanian Ignimbrite units were analyzed via Secondary Ion Mass Spectrometry and electron microprobe. These melt inclusions record H_2O concentrations from near-zero to 3.5 wt%. The most quickly cooled fallout deposits have markedly consistent H_2O concentrations averaging 2.02 ± 0.25 wt%. Ignimbrite flow units record universally low H_2O concentrations < 1 wt%, which we interpret as having been degassed during slow cooling. The highly incompatible trace element Zr serves as a proxy for melt evolution in MI glasses and varies over a factor of six, despite stable H_2O concentrations. We propose that shallow re-equilibration of H_2O in the magma during brief storage at $\sim 2.3 \pm 0.36$ km (460 ± 72 bar) just prior to eruption is responsible for consistent volatile concentrations within the melts that span a relatively large compositional range. Three MI have higher H_2O concentrations at 3.38 ± 0.14 wt% and lower trace element concentrations corresponding to eruption of magmas from deeper portions of the magma system around 4.6 ± 0.35 km (920 ± 70 bar). The magma system is envisaged to be composed of discrete sills at varying depths, which supplied magma to different vents during successive phases of the eruption. Therefore, most melt inclusions do not record the full magmatic volatile history of the Campanian Ignimbrite, but reflect magmatic volatile conditions during a short-lived, shallow storage event during which re-equilibration allowed H^+ to escape from the melt inclusions while H_2O exsolved from the magma, providing exsolved gas for the expanded pyroclastic density current.

Keywords Campi Flegrei · Volatiles · Shallow re-equilibration · Melt inclusions

Introduction

Magmatic volatiles (e.g., H_2O, CO_2, S, and Cl) play an important role in volcanic eruptions and explosivity (e.g., Parfitt and Wilson 2008). As pressure on a magma body decreases during ascent, changes in the concentration and composition of volatiles in the silicate melt control the timing and extent of gas bubble nucleation and growth. The generation of pyroclastic density currents (PDCs), especially dilute (gas-rich and solids-poor) currents, is dependent upon the availability of free gas (e.g., Sparks et al. 1978; Dobran et al. 1993; Koyaguchi et al. 2018; Trolese et al. 2019) and, in particular, on the relative proportion and degassing styles of H_2O and CO_2, which are commonly the two most abundant and important volatile species in a magmatic system.

Assessing the original volatile concentrations of a magma prior to the exsolution of a vapor phase is

Editorial responsibility: M. Edmonds

✉ Michael H. Ort
mtablescrap@gmail.com

✉ Victoria C. Smith
victoria.smith@arch.ox.ac.uk

[1] School of Earth and Sustainability, Northern Arizona University, Flagstaff, AZ 86011, USA

[2] SETI Institute Carl Sagan Center for Research, Mountain View, CA 94043, USA

[3] School of Archaeology, University of Oxford, Oxford OX1, 3TG, UK

[4] Dipartimento Di Scienze- Scienze Geologiche, Universita Di Roma Tre, 00146 Rome, Italy

[5] Istituto Nazionale Di Geofisica E Vulcanologia, Osservatorio Vesuviano, 80124 Naples, Italy

Published online: 15 April 2026

challenging since the *exsolved* volatile component is expelled as gas during eruption (or via diffuse degassing, hydrothermal scrubbing, or fumarolic activity) and is thus not directly recorded in the rock record. The concentration of *dissolved* volatiles present in the melt prior to eruption may be recorded directly in crystal-hosted melt inclusions (MI), microns-scale bits of liquid melt that become entrapped in growing crystals and remain sequestered from volatile loss experienced by intercrystal matrix melt. Interpretation of MI must be done with care, since they may be subjected to post-entrapment, syn-eruptive, and post-eruptive processes that preferentially alter volatile contents while leaving non-volatile geochemistry unchanged. This is particularly challenging in large caldera-forming eruptions like the Campanian Ignimbrite, the subject of this investigation. Post-emplacement hydrogen diffusion out of MI occurs rapidly in slow-cooling units, such as thick ignimbrites and lava flows (e.g., Lowenstern 1995), in which the MI remain at high temperatures for hours to years. Prolonged slow cooling can lead to anomalously low MI H_2O concentrations that reflect emplacement rather than magmatic conditions. Quickly cooled units and deposits emplaced cold, such as fallout, more faithfully record magmatic H_2O concentrations since they are minimally affected by post-emplacement hydrogen diffusion.

In special cases, we can assess pre-eruptive saturation and degassing by comparing the concentrations of volatiles to highly incompatible trace elements in MI (Iacovino et al. 2016). Both volatiles and incompatible trace elements are largely excluded from crystallizing phases and become enriched in the melt during magma differentiation. Fluid exsolution via second boiling occurs when volatile saturation is reached (Blake 1984; Tait et al. 1989). At this point, volatiles can no longer be treated as incompatible. Further crystallization does not increase dissolved volatile concentrations, which instead remain buffered at the saturation limit with excess volatiles instead partitioned into the co-existing vapor phase. Incompatible trace elements that are not soluble in the vapor phase continue to increase even as volatiles stabilize or decrease, as long as the trace element remains incompatible with the crystallizing phase assemblage (e.g., Anderson 1974, 1979; Wallace et al. 1995; Iacovino et al. 2016). Therefore, an increase (or broad variation) in incompatible trace element concentrations with steady volatile content in MI may indicate that the magma reached volatile saturation. If the magma ascends to a lower pressure, then gas will exsolve to reach a lower dissolved gas content in equilibrium with the new pressure while recording the previous evidence of fractionation in the trace element concentrations.

The objective of this study is to describe pre-eruptive conditions (pressure, temperature, and composition) for the Campanian Ignimbrite (CI) eruption by studying clinopyroxene-hosted MI. We present new MI major, trace, and volatile element concentrations from six eruptive units and combine those data with previously published MI data (e.g., Signorelli et al. 1999, 2001; Webster et al. 2003; Fulignati et al. 2004; Marianelli et al. 2006; Severs 2007; Moretti et al. 2019) to gain understanding of the magma storage and processes prior to the CI eruption. We compare the incompatible trace element zirconium (Zr) to MI H_2O concentrations in both quickly and slowly cooled deposits and find that CI magma was probably volatile saturated prior to the 39.8 ka eruption. Consistent H_2O concentrations of ~ 2 wt% over a wide range of Zr contents indicate pre-eruptive magma storage at ~ 2.3 km depth. MI H_2O contents up to 6 wt% in Plinian pumice fallout deposits have been reported in the literature (Marianelli et al. 2006), and so it is likely that MI with ~ 2 wt% were "reset" to this lower value during brief storage in the shallow crust just prior to eruption. Hydrogen diffusion modeling suggests that a period of only 1–2 weeks would be sufficient for MI to re-equilibrate from 6 to 2 wt% H_2O. We propose that the CI underwent a period of shallow storage at ~ 2.3 km depth in a system of extensive sills, where re-equilibration to the saturation limit of H_2O occurred, resulting in the loss of ~ 4 wt% H_2O over the course of 1–2 weeks before erupting. This may have provided the gas for the significant inflation of the PDCs that emplaced the CI deposits.

Geologic background

The CI was emplaced at 39.8 ka (Giaccio et al. 2017) around Naples, Italy, during the largest European eruption of the last 200,000 years. The current eruption volume estimates range between 179 and 243 km^3 dense rock equivalent (DRE) of trachytic-phonolitic magma for the ignimbrite and co-ignimbrite fallout, making it a VEI7 and M7.7 eruption (Silleni et al. 2020). The basal fallout is from an early Plinian column. Plinian fallout volume is estimated between 2 to 22 km^3 DRE (Marti et al. 2016). The CI is found in outcrops throughout the Campanian Plain and adjacent Apennine Mountains (Barberi et al. 1978; Silleni et al. 2020; Fig. 1) and co-ignimbrite fallout is located as far away as Russia (Anikovich et al. 2007; Giaccio et al. 2008; Smith et al. 2016). CI outcrops are also located on the island of Procida and in the Gulf of Naples (Melluso et al. 1995; Fedele et al. 2008; Scarpati et al. 2020) and the ash fallout (Plinian and co-ignimbrite) is present in many marine cores in the Tyrrhenian and Adriatic Seas (Engwell et al. 2014).

The CI eruption began with a ~ 44-km-high Plinian column, depositing the southeastward-distributed Plinian Pumice Fallout (Rosi et al. 1999; Marti et al. 2016). PDCs then emplaced the CI across the Campanian Plain and nearby mountains over an area of ~ 7,000 km^2 (Silleni et al. 2020). A buoyant co-ignimbrite plume developed above PDCs

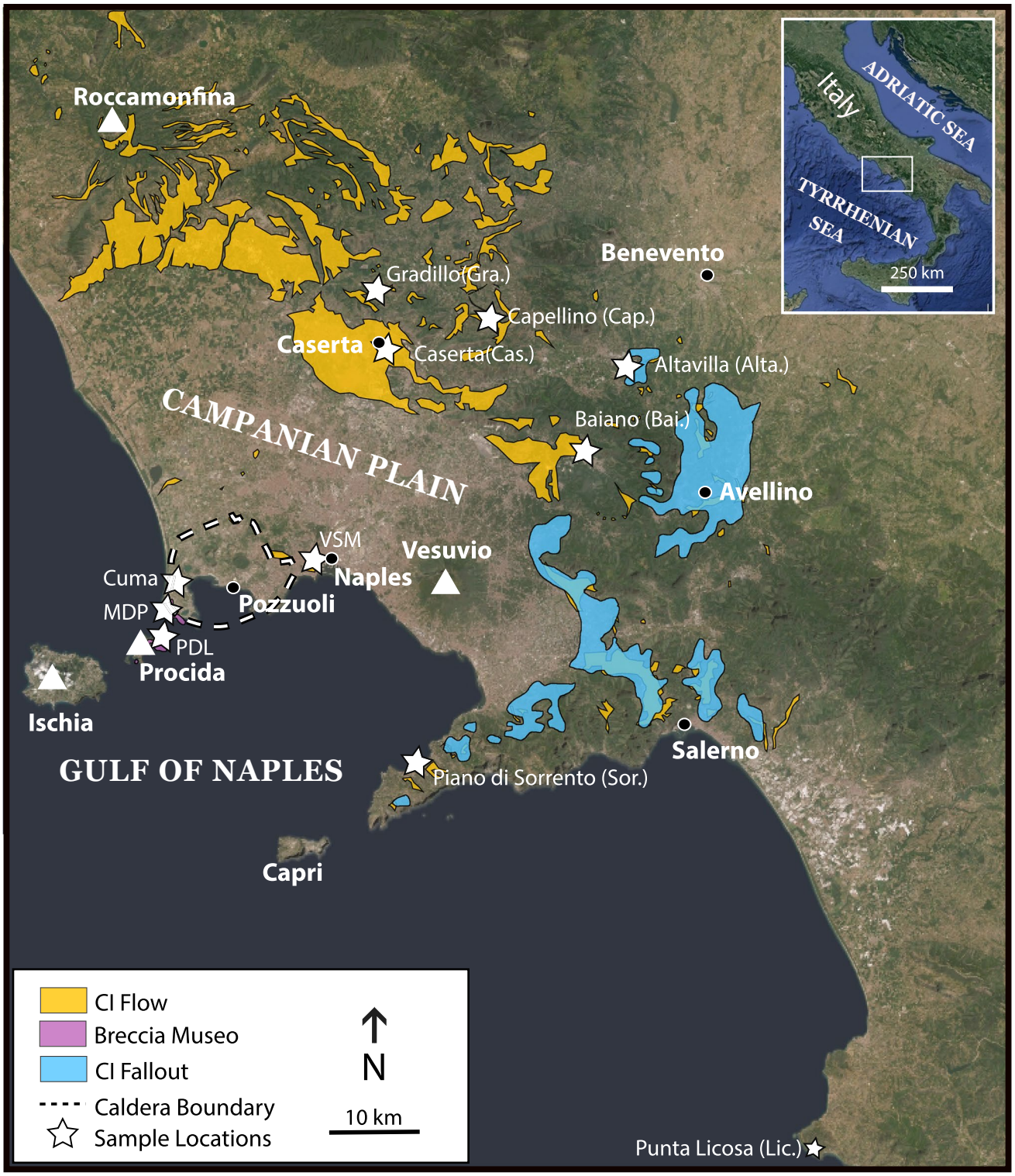

Fig. 1 Satellite map showing the deposits of the Campanian Ignimbrite flow (yellow), fallout (blue), and the proximal Breccia Unit (purple), modified from Silleni et al. (2020), with approximate Campi Flegrei caldera rim from Vitale and Isaia (2014). Sampling locations are marked by filled white stars (VSM = Vigna San Martino, MDP = Monte di Procida, PDL = Punta della Lingua). Cities are shown as black dots, and volcanoes are marked by a white triangle. See Gallo et al. (2024) for grid references of the sampling locations, with the exception of Punta Licosa (40.2330667° N, 14.9273111° E)

and rose into the air to 37 km (Marti et al. 2016) as a large phoenix cloud. This cloud cooled quickly and traveled long distances from the vent before ash settled as a co-ignimbrite fallout deposit across the eastern Mediterranean region and on to Russia (Pyle et al. 2006; Costa et al. 2012; Smith et al. 2016). The two types of fallout are geochemically distinguishable (Smith et al. 2016).

CI PDC deposits overlie the Plinian Pumice Fallout and can be separated into proximal and distal deposits. Here, we adopt the correlation scheme of Gallo et al. (2024), which refines and links the proximal and distal stratigraphy defined by others (Rosi et al. 1996; Fedele et al. 2008, 2016). Additionally, we tie the co-ignimbrite fallout to the main phase of the CI, specifically the distal Welded Gray Ignimbrite and Lithified Yellow Tuff units, a topic explored further in the discussion. In addition to the co-ignimbrite fallout deposits, we focus on three slowly cooled units of the PDC: 1) the proximal Breccia Unit, a coarse lithic-rich breccia containing variable amounts of pumice and obsidian clasts, representing the caldera-collapse phase; 2) the distal Welded Gray Ignimbrite, which is the volumetrically dominant CI unit, and 3) the distal Lithified Yellow Tuff, which is compositionally similar to the Welded Gray Ignimbrite but is distinguished by extensive post-emplacement zeolitization and a distinct lithic clast assemblage (Fedele et al. 2008; Gallo et al. 2024).

Strong evidence exists that the PDCs emplacing the CI were dilute (gas rich and solids poor) from the geographic and temporal start of the eruption (Fisher et al. 1993; Scarpati et al. 2015; Ort et al. 2003, 2018). The PDCs traveled long distances and passed topographic barriers in the Apennine Mountains (> 1400 m high). They flowed over the Gulf of Naples for ~ 30 km with limited interaction with water, implying the flow had a density less than that of water with most material carried high enough in the flow not to interact with the water (Fisher et al. 1993). Additionally, anisotropy of magnetic susceptibility data show that the CI deposit flowed downhill, in many cases directly toward the caldera in the Apennine Mountains, implying that the depositional part of the PDC was influenced strongly by topography and was detached from the transport system (Ort et al. 2003). Proximal breccia deposits show efficient separation of large lithic and pumice clasts from the current, implying it was dilute even close to the vent, and a ground layer is present to distal localities (Scarpati et al. 2015). High emplacement temperatures (> 580 °C; Cappelletti et al. 2003; Ort et al. 2018) indicate the PDC did not cool significantly during transport, so air and water entrainment were limited. Thus, a source for hot gas is needed to explain the dilute nature of the PDC.

Several models of the magma chamber beneath Campi Flegrei have been proposed to account for the variation in $^{87}Sr/^{86}Sr$, $^{143}Nd/^{144}Nd$, and $^{206}Pb/^{204}Pb$ isotopic and geochemical signatures of lavas and tuffs erupted through time (e.g., Civetta et al. 1997; Pappalardo et al. 1999, 2002a; Arienzo et al. 2009, 2011; Forni et al. 2018). Some of these models are for the system present under the modern Campi Flegrei whereas others are for moments in time, such as for the Campanian Ignimbrite magma body. The dominant model for the Campanian Ignimbrite body, based on stratigraphic correlations combined with major- and trace-element geochemistry, suggests it was fed by two magmas, an upper, volatile-rich, more-differentiated and homogenous trachytic-phonolitic melt, and a lower heterogeneous trachytic melt (e.g., Civetta et al. 1997; Signorelli et al. 2001; Pappalardo et al. 2002a, b; Fedele et al. 2008, 2016; Tomlinson et al. 2012; Forni et al. 2016; Smith et al. 2016; Di Salvo et al. 2020; Gallo et al. 2024). Present geophysical data and mineral-phase assemblages for the Campanian Ignimbrite and more recent eruptions suggest a storage zone of melt starting from ~ 9 km depth (e.g., Civetta et al. 1997; Zollo et al. 2008; De Siena et al. 2010; Stock et al. 2018; Isaia et al. 2025).

Previous campanian ignimbrite melt inclusions studies

The CI has been the focus of several MI studies over the past 20 years (Signorelli et al. 1999, 2001; Webster et al. 2003; Fulignati et al. 2004; Marianelli et al. 2006; Severs 2007; Moretti et al. 2019). These studies primarily focused on clinopyroxene-hosted MI, and some of the studies reheated MI (e.g., Webster et al. 2003; Severs 2007), potentially compromising the reported volatile, especially H_2O, concentrations.

H_2O measurements with corresponding major-element compositions have been reported for the Plinian Pumice Fallout (distinct populations with ~ 2–3 and 5–6 wt%; Marianelli et al. 2006), Welded Gray Ignimbrite (wide range from 0.41–4.20 wt%; Marianelli et al. 2006; Moretti et al. 2019), and Breccia Unit (wide range from 0.92–5.77 wt%; Marianelli et al. 2006; Severs 2007). CO_2 concentrations in MI from the Welded Gray Ignimbrite and Breccia Unit are mostly below detection limit, with one MI from an ignimbrite unit containing 214 ppm (Moretti et al. 2019) and three Breccia Unit MI containing 200–500 ppm (Severs 2007).

Sample selection and preparation

Clinopyroxene-hosted melt inclusions were measured in six rock units: the Welded Gray Ignimbrite and the Lithified Yellow Tuff and their associated co-ignimbrite fallout, the Breccia Unit, the Plinian Pumice Fallout, and the Unconsolidated Stratified Ash Flow. Eleven sample sites were chosen in six distal and five proximal locations based on geographic spread and sections where multiple units were

exposed (Fig. 1). The ignimbrite/breccia/tuff units (including the ash-flow deposit) were emplaced at high temperatures (> 580 ºC based on thermal magnetisation, Cappelletti et al. 2003, Ort et al. 2018; ~ 675 ºC based on shard deformation experiments, Silleni 2019) and then slowly cooled. The co-ignimbrite fallout, which we consider coeval with the Welded Gray Ignimbrite and Lithified Yellow Tuff (the current that deposited the ignimbrite rose into the air and distributed the co-ignimbrite fallout), cooled quickly when the PDC lofted into the phoenix cloud. The early Plinian Pumice Fallout is interpreted to be the most quickly cooled of all deposits studied and so most likely to preserve pre-eruptive volatile contents in MI.

MI observed in our samples are almost exclusively hosted in clinopyroxene, consistent with other MI studies of the CI (Signorelli et al. 1999, 2001; Webster et al. 2003; Fulignati et al. 2004; Marianelli et al. 2006; Severs 2007; Moretti et al. 2019), and so only clinopyroxene phenocrysts were chosen for analysis. Crystals were separated from whole-rock samples via crushing, heavy liquid separation, and a magnetic separator. Crystals were then handpicked from the −1 to 1 Φ fractions, and individually mounted on glass slides with CrystalBond and polished with sandpaper of grits 1000 and 2000, and diamond polishing sheets of grits 3 and 1 µm to expose individual MI.

Transmitted- and reflected-light microscopy were used to target MI that were large (> 35 µm), glassy, bubble free, and fully enclosed. These parameters were chosen to minimize uncertainty caused by post-entrapment processes (Lowenstern 1995). A total of 60 MI were selected for analysis (later filtered to 51; see Sect. "Data filtering").

After polishing and high-grading, acetone was used to dissolve the CrystalBond and release the clinopyroxene grains. Grains with exposed MI were then mounted for Electron Micro-Probe (EMPA) and Secondary Ion Mass Spectrometer (SIMS) analyses. Indium was chosen as a mounting medium because it does not degas under instrument vacuum, making indium a better medium than epoxy, especially when analyzing hydrogen. Indium was heated to ~ 160 °C and the melted metal was poured into an aluminum disk 2.54 cm in diameter. The mount was pressed, creating a smooth surface of indium. Troughs were then gouged into the indium to make room for the clinopyroxene crystals, which were then placed into the troughs. The mount was pressed after each crystal was inserted to ensure the crystal was sitting at the surface and in a horizontal orientation. Excess indium was then used to backfill the mount and create a smooth, level surface. A previously prepared (and fully degassed) epoxy mount of clinopyroxene from the Plinian Pumice Fallout was also analyzed and produced results consistent with those on the indium mount.

Analytical methods

Major elements, S, and Cl

EMPA analyses of MI were carried out on a JEOL JXA-8200 at the University of Oxford to determine major elements, Cl, and S concentrations of 60 MI and major elements in 27 host clinopyroxene phenocrysts. MI analyses were run near the spots chosen for SIMS (i.e., adjacent to SIMS pits) using an 8 µm beam diameter at either 15 kV and 6 nA for major elements or 15 kV and 20 nA for S and Cl. Clinopyroxene host crystals were analyzed adjacent to and in the same zone (where applicable) as the MI using a 3 µm beam diameter at 15 kV and 15 nA. The calibration was verified by running reference materials as secondary standards during each analytical run.

H_2O and trace element analysis

SIMS analyses of MI were carried out on a Cameca ims6f instrument at Arizona State University. An O_2^- primary ion beam of ~ 10 µm with a raster size of 20 µm was used, along with energy filtering that involves decreasing the voltage from 9000 EV ± 20 during analysis (Hervig et al. 2003). A total of 60 MI were analyzed for H, Rb, Y, Zr, Nb, Ce, Nd, and Eu. Some MI were also measured for La, Pr, Sm, Ta, Th, and U. The analyses were calibrated using the standards NIST610, NIST612, M3N, M6N, and 092. Before, during, and after analysis, the standards were checked and used to make calibration curves for each element. Mean value, standard deviation, mean standard error, Poisson error, rejected number, and integrated mean were calculated for each element analyzed. Errors were then calculated for each element/Si by multiplying the standard error by the element/Si divided by 100. Errors were propagated with standard deviation of Si from EMPA once the SIMS data were converted to ppm.

Data filtering

Our dataset of 60 measured MI was rigorously filtered to remove any analyses that inadvertently included either the clinopyroxene host or MI daughter crystals in the analysis volume, resulting in 33 major, S, and Cl compositions; 49 trace element and H_2O compositions; and 51 total MI compositions. Electron backscatter images were used to target crystal-free spots, but crystals below the surface of the charge may still be included in the analysis volume, particularly for very small (< 50 µm) MI. Due to instrument availability, SIMS measurements (H_2O and trace

elements) were performed first before EPMA measurements (major elements, S, and Cl), which were targeted adjacent to SIMS pits. Since a crystal could be included in the major element analysis but not the trace element analysis and vice versa, we filter the data set separately for major elements (plus S and Cl) and for trace elements (plus H_2O).

Major-element compositions deemed contaminated by clinopyroxene (MgO > 10 wt%; FeO > 5 wt%) or apatite inclusions (CaO/FeO > 3; CaO > 4 wt%, P_2O_5 > 1 wt%) were removed from the dataset. Trace-element compositions with Y/Zr > 0.35 were deemed contaminated by apatite and removed from the dataset. Finally, analyses with low analytical totals were removed. Literature data used to compare to our dataset were filtered using the same criteria.

Results

Clinopyroxene compositions

All MI analyzed in this study are hosted in clinopyroxene phenocrysts. Analyses of clinopyroxene crystals taken adjacent to their MI are reported in Table 1. The clinopyroxene crystals all classify as diopside, and span the same range of colors and compositions recognized in other CI studies (e.g., Fedele et al. 2008; Forni et al. 2016). The light green crystals classify as Mg-rich diopside, and their compositions fall within the Type-1 group of Forni et al. (2016) with Mg# (Mg/[Mg+Fe]*100) ranging from 81 to 91 and $En_{48–51}Fs_{2–7}Wo_{42–49}$ (n = 11). These light crystals do not typically contain accessory phases or MI. The darker green to black population, spanning type 2–3 compositional populations of Forni et al. (2016), have Mg# 67–77 and $En_{37–42}Fs_{6–11}Wo_{49–53}$ (n = 51). Given these clinopyroxene compositions do not clearly fall into discrete type 2 and 3 groups of Forni et al. (2016), with analyses plotting between the two groups, we have combined the analyses that plot within and between the groups together into "type 2–3". These dark type 2–3 crystals have abundant MI of a range of sizes and commonly have apatite and magnetite inclusions (Table 2).

Type 1 crystals are observed in both the Plinian Pumice Fallout and the Breccia Unit, and all units contain the type 2–3 crystals. All clinopyroxene compositions are reported in Table 1.

Melt inclusion compositions

All major, trace, and volatile concentrations measured in 51 MI glasses are reported in Table 2. Average compositions for each unit are in Table 3. The MI are hosted in clinopyroxene crystals from six units sampled from 11 unique localities (Fig. 1). Due to logistical constraints posed by the Covid-19 pandemic, not all samples were measured both by EMPA (major ± S and Cl) and SIMS (H_2O and trace). Twenty-five samples have EMPA measurements (majors ± S and Cl), 49 have SIMS measurements (trace and H_2O), and 23 samples have both EMPA and SIMS measurements.

Major element concentrations

All clinopyroxene-hosted MI have glass compositions ranging from 60.7–63.8 wt% SiO_2 and 10.4–15.1 wt% total alkalis, consistent with the range of values reported in the existing CI literature (Fig. 2; Signorelli et al. 1999; Webster et al. 2003; Fulignati et al. 2004; Marianelli et al. 2006; Severs 2007; Moretti et al. 2019; Table S1). MI can be compositionally separated into two groups, a high-Na_2O group and a low-Na_2O group (Fig. 3), as is seen in the matrix glass (Smith et al. 2016; Gallo et al. 2024). The MI show weak general trends of decreasing Al_2O_3, CaO, FeO, and TiO_2 with increasing SiO_2 concentrations (Fig. 3). There is no correlation of major-element oxides with measured MI concentrations of water, chlorine, or sulfur (Supplementary Fig. S1, S2, S3, S4). MI in the Plinian Pumice Fallout and co-ignimbrite fallout are dominantly trachytic. Welded Gray Ignimbrite and Lithified Yellow Tuff MI in this study are trachytic to phonolitic. Breccia Unit MI in our dataset are trachytic to trachyandesitic (Fig. 2).

Trace element concentrations

Several trace elements were analyzed in the MI and are reported in Table 2 and Fig. 4: high field-strength elements (HFSE; Zr, Nb, Ta, U, Th) and large-ion lithophile elements (LILE; Rb, Eu), and rare earth elements (REE; Y, Ce, Nd, La, Pr, Sm). Zr shows high incompatibility in our measured MI, so we use Zr as a proxy for magma evolution. The Zr concentrations in the Plinian Pumice Fallout form two populations, a low-Zr (85–201 ppm) and a high-Zr (373–599 ppm) group (Fig. 4). Co-ignimbrite fallout Zr concentrations are mainly in the high-Zr group with only one < 100 ppm. Our single acceptable analysis of Unconsolidated Stratified Ash Flow Zr concentration is 204 ppm. Welded Gray Ignimbrite, Lithified Yellow Tuff, and BU Zr concentrations vary from 56–407 ppm.

Rb concentrations cluster around ~ 200 ppm with the tightest clustering in the PPF unit, averaging 224 ppm (low-Zr MI) and 304 ppm (high-Zr MI). LYT samples have the lowest Rb contents at 27 and 126 ppm and WGI samples have a maximum of 418 ppm Rb (Fig. 4). Eu concentrations vary significantly within eruptive units, with PPF MI spanning < 2–8 ppm with no correlation to SiO_2, H_2O, or Cl. Analyzed rare-earth elements (REE) include Y, Ce, Nd, Eu,

Table 1 Compositions of clinopyroxene host crystals (wt%) measured adjacent to their MI via EPMA. Analytical errors (1 standard deviation; wt%) are as follows: 0.10 SiO_2, 0.02 TiO_2, 0.03 Al_2O_3, 0.06 FeO, 0.02 MnO, 0.04 MgO, 0.05 CaO, and 0.02 Na_2O. Unit abbreviations as in Fig. 2 and text, and the sampling locations are in Fig. 1

Sample	C19-1B	C19-1B	CI-S6	CI-S6	CF321	CF321	CF321	CF321	CF321	CF321	CF321	CF321	CF321	CF321	CF321	CF321
Crystal	1-1	1-3	2-5	2-9	1-1	1-2	1-5	1-6	1-21	1-22	1-23	1-43	1-45	1-48	1-56	1-60
Location	Cuma	Cuma	Bai.	Bai.	VSM	VSM	VSM	VSM	VSM	VSM	VSM	VSM	VSM	VSM	VSM	VSM
Unit	PPF	PPF	PPF	PPF	PPF	PPF	PPF	PPF	PPF	PPF	PPF	PPF	PPF	PPF	PPF	PPF
SiO_2	52.31	50.01	50.3	51.58	50.23	50.18	50.3	49.92	49.02	50.17	49.57	49.67	50.46	50.78	50.56	50.37
TiO_2	0.36	0.58	0.5	0.48	0.49	0.54	0.52	0.51	0.76	0.51	0.62	0.57	0.62	0.63	0.74	0.67
Al_2O_3	2.43	3.64	3.57	2.89	3.96	3.58	3.27	3.57	4.83	3.55	4.26	3.99	2.65	2.45	4.05	2.55
FeO	6.05	8.34	8.3	5.26	8.07	8.27	8.47	8.31	8.69	8.16	8.23	8.25	9.5	9.69	5.08	9.96
MnO	0.17	0.36	0.3	0.13	0.31	0.38	0.35	0.37	0.29	0.31	0.2	0.25	0.82	0.85	0.12	0.83
MgO	14.39	13.45	13.37	15.58	13.62	13.32	13.61	13.55	12.77	13.66	13.53	13.71	12.27	12.02	15.18	11.94
CaO	23.83	23.28	23.35	23.91	22.93	23.36	23.15	23.41	23.32	23.29	23.34	23.27	22.93	22.85	23.94	22.95
Na_2O	0.39	0.3	0.31	0.14	0.37	0.37	0.31	0.36	0.31	0.33	0.23	0.26	0.71	0.71	0.2	0.72
Total	99.93	99.96	100.00	99.97	99.98	100.00	99.98	100.00	99.99	99.98	99.98	99.97	99.96	99.98	99.87	99.99
Mg#	70.4	61.73	61.7	74.77	62.8	61.7	61.64	62	59.5	62.62	62.19	62.43	56.35	55.38	74.93	54.51
Wo	50.16	50.93	50.84	49.97	50.25	51.29	50.46	51.61	51.93	50.96	51.11	51.07	51.77	51.26	51.12	51.95
En	42.15	40.96	40.51	45.29	41.54	40.68	41.26	41.57	39.55	41.59	41.24	41.87	38.53	37.53	45.1	37.6
Fs	7.69	8.11	8.66	4.74	8.21	8.03	8.28	6.81	8.52	7.45	7.65	7.06	9.7	11.21	3.79	10.45
Sample	C19-3B	C19-40B	C19-40B	C19-40C	C19-40C	C19-40C	C19-16	C19-16	C19-16	C19-21	C19-17C	C19-17C	C19-17D	C19-17G	CI-S5	CI-S5
Crystal	2-1	1-1	1-2	1-1	1-2	1-3	1-2	3-2	3-3	1-1	2-1	4-3	1-1	1-1	1-2	3-1
Location	MDP	PDL	PDL	PDL	PDL	PDL	Cas.	Cas.	Cas.	Cap.	Gra.	Gra.	Gra.	Gra.	Lic.	Lic.
Unit	BU	BU	BU	BU	BU	BU	LYT	LYT	LYT	LYT	WGI	WGI	WGI	WGI	Co-ig	Co-ig
SiO_2	50.28	50.26	50.62	50.49	50.43	50.84	50.81	50.77	50.79	50.38	51.32	50.82	50.35	50.77	50.57	50.37
TiO_2	0.99	0.53	0.58	0.53	0.51	0.53	0.54	0.57	0.57	0.54	0.5	0.67	0.58	0.64	0.48	0.62
Al_2O_3	3.94	3.03	2.46	3	3.16	2.72	3.3	3.15	2.97	3.54	2.65	2.56	4.32	2.64	3.43	2.41
FeO	7.53	9.24	9.5	8.71	8.84	8.84	8.44	8.77	8.43	8.33	8.52	9.57	8.22	9.07	8.19	9.93
MnO	0.2	0.63	0.72	0.48	0.5	0.5	0.41	0.49	0.52	0.35	0.54	0.76	0.31	0.73	0.26	0.92
MgO	14.08	12.77	12.5	13.01	12.96	12.98	13.15	12.49	13.03	13.44	12.81	12.23	13.05	12.38	13.61	12.04
CaO	22.62	23.08	23.03	23.4	23.2	23.15	22.94	23.24	23.23	23.08	23.17	22.83	22.89	23.05	23.15	23.03
Na_2O	0.31	0.44	0.58	0.37	0.36	0.41	0.41	0.5	0.46	0.33	0.43	0.54	0.28	0.63	0.29	0.68
Total	99.95	99.98	99.99	99.99	99.96	99.97	100.00	99.98	100.00	99.99	99.94	99.98	100.00	99.91	99.98	100.00
Mg#	65.13	58.02	56.82	59.91	59.46	59.5	60.89	58.75	60.71	61.75	60.06	56.1	61.34	57.72	62.44	54.79
Wo	48.82	51.1	51.2	51.11	50.77	50.42	49.86	50.98	50.78	50.27	50.21	50.34	49.63	51.22	62.44	54.79
En	42.27	39.32	38.65	39.55	39.46	39.34	39.75	38.11	39.63	40.73	38.62	37.54	39.35	38.29	50.04	52.05
Fs	8.91	9.58	10.16	9.34	9.77	10.24	10.39	10.91	9.59	9.01	11.16	12.12	11.02	10.49	40.92	37.85

Table 2 Major, trace, and volatile concentrations measured in 51 MI glasses via EMPA and SIMS. Major elements are normalized to 100% anhydrous with original EMPA totals given. Due to logistical constraints posed by the Covid-19 pandemic, not all samples were measured both by EMPA (major±S and Cl) and SIMS (H_2O and trace). 25 samples have EPMA measurements (majors±S and Cl), 49 have SIMS measurements (trace and H_2O), and 23 samples have both EPMA and SIMS measurements. Medium = mounting medium. Descriptions of the MI are also included; Sub-cir.=sub-circular; MI crystals = daughter crystals within the MI of unknown composition, and Cracks = fractures in the host crystal surrounding the MI. Unit abbreviations as in Fig. 2 and text, and see Fig. 1 for sampling locations.

Sample	CF321	CF321	CF321	CF321	CF321	CF321	CF321	CF321	CF321	CF321	CF321	CF321	CF321	CF321	CF321	CF321	CF321	CF321	CF321	CF321	CF321	CF321	CF321	CF321	CI-S6-2	CI-S6-2	C19-16
Crystal	1-1	19-1	2-1	21-2	21-2b	21-3	21-4	22-1	23-1	3-1	3-2	3-3	43-1	45-1	48-1	49-1	5-1	56-1	56-2	56-4	56-6	6-2	60-1	5	9	03-3
Location	VSM	VSM	VSM	VSM	VSM	VSM	VSM	VSM	VSM	VSM	VSM	VSM	VSM	VSM	VSM	VSM	VSM	VSM	VSM	VSM	VSM	VSM	VSM	Bai.	Bai.	Cas.
Unit	PPF	PPF	PPF	PPF	PPF	PPF	PPF	PPF	PPF	PPF	PPF	PPF	PPF	PPF	PPF	PPF	PPF	PPF	PPF	PPF	PPF	PPF	PPF	PPF	PPF	LYT
(wt%)																										
SiO_2			61.22	61.62	61.62	61.50	61.60	61.81	61.91	61.24	61.41	60.65	60.91		61.55		62.67		61.00			61.61		61.24	60.73	61.82
TiO_2			0.33	0.32	0.32	0.30	0.37	0.43	0.23	0.46	0.43	0.43	0.40		0.45		0.49		0.41			0.40		0.44	0.25	0.52
Al_2O_3			19.84	18.96	18.96	18.75	18.87	18.79	19.74	18.45	18.10	18.38	19.13		18.97		17.99		19.18			18.46		19.07	20.17	18.32
FeO			2.94	3.41	3.41	3.37	3.47	3.19	2.68	3.72	3.81	3.79	3.57		3.13		3.38		3.29			3.45		3.28	2.61	2.58
MnO			0.19	0.09	0.09	0.09	0.07	0.08	0.09	0.10	0.13	0.16	0.13		0.25		0.19		0.10			0.15		0.09	0.03	0.18
MgO			0.34	0.43	0.43	0.44	0.39	0.48	0.30	0.44	0.71	0.84	0.49		0.28		0.26		0.37			0.58		0.40	0.45	0.51
CaO			1.65	1.84	1.84	2.12	1.77	1.92	2.40	2.51	2.27	2.72	1.94		1.66		1.48		1.94			2.13		2.06	3.01	2.28
Na_2O			5.80	3.11	3.11	3.27	2.66	3.03	3.55	3.16	3.01	3.10	3.10		6.32		3.52		3.31			3.09		3.55	3.72	3.59
K_2O			7.66	10.06	10.06	10.01	10.62	10.10	9.05	9.74	10.01	9.77	10.18		7.36		9.88		10.22			10.01		9.74	8.80	10.11
P_2O_5			0.02	0.16	0.16	0.16	0.17	0.17	0.06	0.18	0.12	0.15	0.16		0.04		0.14		0.18			0.13		0.13	0.25	0.09
H_2O	1.50	1.73	2.30	1.56	1.61	2.29	1.94	2.05	2.42	1.87	1.96	1.98	2.25	2.27	2.03	2.24		1.68	2.12	2.24	1.68	2.26	1.88	2.11	2.25	0.84
Total			95.82	96.40	96.40	95.93	95.01	95.94	95.87	96.47	96.01	96.89	95.55		95.28		96.73		95.27			93.62		94.27	91.48	93.71
(ppm)																										
S			162	488	488	394	381	582	63	462	552	471	155		209		360		549			473		143	54	206
Cl			8216	3613	3613	3735	3744	3688	4846	3687	3381	3387	3763		8384		3956		3668			3815		4041	6072	1609
Rb	152	241	346	251	257	240	260	241	209	212	214	218	222	314	356	193		162	217	153	312	227	264	233	205	126
Y	37	51	40	17	19	18	17	17	16	21	20	19	17	39	51	11		14	28	7	44	21	79	18	9	45
Zr	259	424	373	169	173	161	161	159	170	170	201	164	151	430	599	133		117	152	85	124	201	478	179	162	325
Nb	43	66	97	26	27	25	27	26	29	24	25	25	24	86	107	21		18	24	18	25	26	79	29	32	46
Ce	97	148	168	71	73	75	68	71	74	75	74	69	68	165	201	46		48	118	32	148	79	342	74	56	146
Nd	58	21	86	9	9	10	8	9	8	42	41	39	9	18	22	5		7	18	4	30	10	50	8	6	19
Eu	2	1	1	5	6	5	7	7	7	7	6	6	6	1	1	3		3	7	4	9	4	3	4	3	2
La																								40	35	72
Pr																								8	6	17
Sm																								1	0	1
Ta																								1	2	2
Th																								12	14	19
U																								4	5	6
Medium	Epoxy	Epoxy	Epoxy	Epoxy	Epoxy	Epoxy	Epoxy	Epoxy	Epoxy	Epoxy	Epoxy	Epoxy	Epoxy	Epoxy	Epoxy	Epoxy	Epoxy	Epoxy	Epoxy	Epoxy	Epoxy	Epoxy	Epoxy	Indium	Indium	Indium
MI Size (μm)	30 × 15	31 × 31	60 × 30	83 × 83	124 × 104	125 × 125	125 × 104	144 × 115	122 × 30	63 × 42	106 × 106	318 × 148	84 × 70	54 × 54	117 × 44	95 × 32	93 × 47	45 × 15	76 × 76	121 × 76	45 × 15	67 × 45	82 × 33	47 × 38	41 × 36	93 × 44
MI Location	Rim	Rim	Core	Rim	Rim	Core	Core	Core	Core	Rim	Rim	Rim	Core	Core	Rim	Core	Rim	Rim	Rim	Rim	Core	Core	Rim	Rim	Core	Rim
MI crystals	None	None	None	None	None	None	None	None	None	None	None	None	None	None	None	None	None	None	None	None	None	None	None	None	None	Apatite
Bubble	No	No	Yes	No	No	No	No	No	No	Yes	Yes	Yes	No	No	No	No	Yes	No	No	No	No	No	No	No	No	No
Shape	Irregular	Irregular	Irregular	Circular	Circular	Circular	Circular	Circular	Elongate	Circular	Irregular	Elongate	Circular	Sub-cir.	Elongate	Irregular	Irregular	Circular	Irregular	Circular	Circular	Circular	Circular	Circular	Circular	Sub-cir.
Cracks	No	No	No	No	No	No	No	No	No	No	No	No	No	No	No	No	No	No	No	No	No	No	No	No	No	No

Table 2 (continued)

Sample	C19-21	Cl9-1B	C19-1B	C19-3B	C19-40B	C19-40B	C19-40C	C19-40C	C19-40C	C18-3A2	C19-17D	C19-17G	C19-27C	C19-27C	C19-35B	C19-35C	C19-35E	CI-S5-1	CI-S5-1	CI-S5-1	CI-S5-1	CI-S5-2	CI-S5-2	CI-S5-3	CI-S5-5
Crystal	01-1	1-1	1-3	2-1	1-1	1-2	1-1	1-2	1-3	2-1	1-1	1-1	1-2	1-4	1-1	1-1	1-3	1	3	4	5	1	2	1	3
Location	Cap.	Cuma	Cuma	MDP	PDL	PDL	PDL	PDL	PDL	Alta.	Gra.	Gra.	Alta.	Alta.	Sor.	Sor.	Sor.	Lic.	Lic.	Lic.	Lic.	Lic.	Lic.	Lic.	Lic.
Unit	LYT	BU	BU	BU	BU	BU	BU	BU	BU	USAF	WGI	WGI	WGI	WGI	WGI	WGI	WGI	Co-ig	Co-ig	Co-ig	Co-ig	Co-ig	Co-ig	Co-ig	Co-ig
(wt%)																									
SiO_2	63.81				62.57	63.04	62.27	61.92			63.48													61.72	
TiO_2	0.29				0.47	0.44	0.45	0.44			0.14													0.41	
Al_2O_3	20.59				18.47	17.44	17.93	18.18			19.49													19.19	
FeO	1.25				3.83	2.86	3.46	3.49			1.44													3.20	
MnO	0.03				0.18	0.18	0.19	0.16			0.00													0.23	
MgO	0.65				0.51	0.36	0.61	0.61			0.03													0.26	
CaO	2.90				2.63	1.79	2.39	2.35			0.22													1.82	
Na_2O	8.36				3.87	3.14	3.48	3.55			2.19													6.12	
K_2O	2.01				7.38	10.68	9.06	9.25			12.92													7.03	
P_2O_5	0.11				0.10	0.07	0.16	0.06			0.08													0.01	
H_2O	0.80	3.43	0.82	1.20	0.86		1.97	1.91	3.49	2.84	0.30	0.19	0.09	0.07	0.05	0.81	0.67	0.89	2.16	2.38	3.23	1.90	1.84	2.23	1.05
Total	96.61				97.76	98.73	96.74	97.19			95.80													96.18	
(ppm)																									
S	558				726	272		291			995													163	
Cl	3633				4121	1173	3445	3285			197		515	3769	221		6967	8110	7278			8340	8601	8064	
Rb	27	232	62	203	244		215	215	180	238	221	217	234	252	394	223	418	139	272	322	177	257	289	356	143
Y	17	12	6	36	57		31	30	22	24	3	11	4	9	48	28	18	84	37	25	12	21	50	51	106
Zr	166	180	57	216	407		299	285	169	204	56	179	63	119	341	278	203	410	360	363	87	197	453	600	320
Nb	25	32	9	36	39		30	29	23	44	6	18	6	16	3	36	65	38	83	96	18	64	84	106	36
Ce	74	54	32	119	265		125	103	73	119	9	46	21	47	98	108	184	171	141	130	66	96	159	200	365
Nd	9	5	4	17	30		16	14	10	15	1	6	2	5	23	14	19	35	16	12	8	10	22	21	64
Eu	2	3	2	8	2		4	4	4	8	4	0	5	4	2	2	2	3	1	1	5	1	1	1	4
La	42	33	21	58	139		61	52	40		9	23												107	
Pr	7	5	3	15	28		14	11	8		1	5												21	
Sm	0	0	0	1	2		1	1	1		0	0												1	
Ta	1	1	0	3	3		2	2	1		0	1												3	
Th	10	19	3	11	31		13	16	11		4	10												42	
U	3	7	1	3	8		4	4	3		2	4												15	
Medium	Indium	Indium	Indium	Indium	Indium	Indium	Indium	Indium	Indium	Indium	Indium	Indium	Indium	Indium	Indium	Indium	Indium	Indium	Indium	Indium	Indium	Indium	Indium	Indium	Indium
MI Size (μm)	63 ×72	55 × 40	52 ×28	95 × 75	104 × 33	70 × 61	71 × 41	81 × 47	55 × 44	197 × 78	70 × 58	50 × 22	119 × 117	351 × 273	114 × 69	76 × 51	118 × 59	45 × 27	82 × 82	149 × 33	132 × 66	116 × 50	153 × 57	95 × 19	37 × 28
MI Location	Rim	Core	Rim	Rim	Core	Core	Rim	Rim	Rim	Core	Core	Core	Core	Core	Core	Core	Core	Core	Rim	Core	Core	Core	Rim	Core	Rim
MI crystals	None	None	None	Apatite	None	Yes*	None	Apatite	Apatite	None	None	None	None	Yes*	None	None	None	Apatite	None	None	None	None	None	None	None
Bubble	No	No	No	No	No	No	No	No	No	No	No	No	No	No	No	No	No	No	No	No	No	No	No	No	Yes
Shape	Circular	Irregular	Sub-cir.	Irregular	Sub-cir.	Circular	Sub-cir.	Sub-cir.	Circular	Irregular	Circular	Circular	Circular	Circular	Irregular	Circular	Circular	Sub-cir.	Circular	Elongate	Irregular	Circular	Sub-cir.	Sub-cir.	Elongate
Cracks	No	Yes	Yes	No	No	No	No	No	No	No	Yes	No	No	No	No			No	No	No	No	No	No	No	No

Table 3 Average melt inclusion glass compositions (wt%) for each unit and all units combined. 1σ standard deviation is given in brackets. Measured H_2O values and corresponding modeled pressures and depths of magma storage are split into "shallow" and "deep" storage regions, as defined in the text. n = number of samples in average and standard deviation. Pressures were modeled assuming 50 ppm CO_2 and 950 °C using VESIcal (Iacovino et al. 2021) with the H_2O-CO_2 solubility model MagmaSat (Ghiorso and Gualda 2015) using individual major element compositions and volatile compositions for each MI. Temperatures used for calculating pressures were those modeled using cpx-liquid thermobarometry (Masotta et al. 2013). Values for each individual sample are given in Supplementary Tables S2 and S3

	PPF		BU		WGI		LYT		Co-ig		All units	
SiO_2	61.35	*(0.37)*	62.25	*(0.33)*	63.28	*(1.79)*	62.81	*(1.41)*	61.50	*(0.99)*	61.93	*(1.12)*
TiO_2	0.37	*(0.07)*	0.45	*(0.01)*	0.19	*(0.04)*	0.40	*(0.17)*	0.38	*(0.03)*	0.36	*(0.10)*
Al_2O_3	18.99	*(0.55)*	18.20	*(0.27)*	19.33	*(1.88)*	19.46	*(1.60)*	19.92	*(1.58)*	19.06	*(1.14)*
FeO	3.32	*(0.35)*	3.59	*(0.20)*	1.59	*(0.50)*	1.92	*(0.94)*	2.64	*(0.67)*	2.88	*(0.81)*
MnO	0.11	*(0.05)*	0.17	*(0.02)*	0.04	*(0.06)*	0.10	*(0.11)*	0.18	*(0.03)*	0.12	*(0.07)*
MgO	0.46	*(0.15)*	0.58	*(0.06)*	0.71	*(0.90)*	0.58	*(0.10)*	0.62	*(0.53)*	0.53	*(0.40)*
CaO	2.11	*(0.39)*	2.45	*(0.15)*	1.54	*(0.80)*	2.59	*(0.43)*	2.05	*(0.81)*	2.05	*(0.57)*
Na_2O	3.56	*(1.01)*	3.63	*(0.20)*	4.48	*(1.64)*	5.97	*(3.38)*	6.06	*(1.35)*	4.21	*(1.56)*
K_2O	9.59	*(0.92)*	8.56	*(1.03)*	8.76	*(2.80)*	6.06	*(5.73)*	6.60	*(0.58)*	8.74	*(2.05)*
P_2O_5	0.14	*(0.06)*	0.11	*(0.05)*	0.08	*(0.07)*	0.10	*(0.01)*	0.06	*(0.05)*	0.11	*(0.06)*
Shallow												
H_2O (wt%)	2.01	*(0.27)*	1.94	*(0.04)*	--	--	--	--	2.10	*(0.23)*	2.02	*(0.25)*
Pressure (bar)	460	*(77)*	430	*(14)*	--	--	--	--	476	*(56)*	460	*(72)*
Depth (km)	2.30	*(0.39)*	2.15	*(0.07)*	--	--	--	--	2.38	*(0.28)*	2.3	*(0.36)*
n	24		2						5		31	
Deep												
H_2O (wt%)	--	--	3.46	*(0.04)*	--	--	--	--	3.23	--	3.38	*(0.14)*
Pressure (bar)	--	--	940	*(14)*	--	--	--	--	820	--	920	*(70)*
Depth (km)	--	--	4.70	*(0.07)*	--	--	--	--	4.10	--	4.6	*(0.35)*
n			2						1		3	

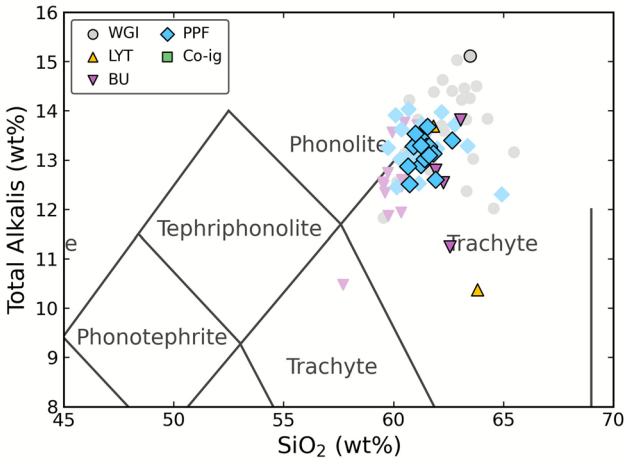

Fig. 2 Total alkalis versus silica (TAS) diagram using the classification scheme of Le Maitre et al. (2002) of melt inclusions measured in this study (bold symbols with black outlines) and those from published literature (faded symbols with no outlines). Literature CI melt inclusion data are from Signorelli et al. (1999), Webster et al. (2003), Fulignati et al. (2004), Marianelli et al. (2006), Severs (2007), and Moretti et al. (2019). Gray circles: Welded Gray Ignimbrite (WGI); yellow triangles: Lithified Yellow Tuff (LYT); purple downward triangles: Breccia Unit (BU); blue diamonds: Plinian Pumice Fall (PPF); green squares: co-ignimbrite fallout (co-ig)

La, Pr, and Sm. The concentrations of these elements are variable, but the scattered pattern and locations of individual samples on plots are generally similar to one another. MI that show enriched Y, Ce, Nd, and Eu likely correspond to overlap on a daughter phase in the MI, such as an apatite microphenocryst, and were excluded from the dataset (Fig. S4).

Volatile concentrations

H_2O, Cl, and S concentrations in MI were measured by SIMS (H_2O) and EMPA (Cl, S; Table 2). H_2O concentrations across all samples generally fall into three groups (Fig. 4; Table S2): low-H_2O (< 1 wt%, $n = 12$), moderate-H_2O (2.02 ± 0.25 wt%, $n = 31$), and high-H_2O (3.38 ± 0.14 wt%, $n = 3$). Low-H_2O samples include all Welded Gray Ignimbrite, all Lithified Yellow Tuff, one Breccia Unit, and one co-ignimbrite MI analyses. Moderate-H_2O samples include all Plinian Pumice Fall, five co-ignimbrite, and two BU MI analyses. High-H_2O samples include one co-ignimbrite and two BU MI analyses. Additionally, one BU and one co-ignimbrite sample fall in between low- and moderate-H_2O groups and our single MI from the Unconsolidated Stratified Ash Flow unit falls between moderate and high-H_2O groups.

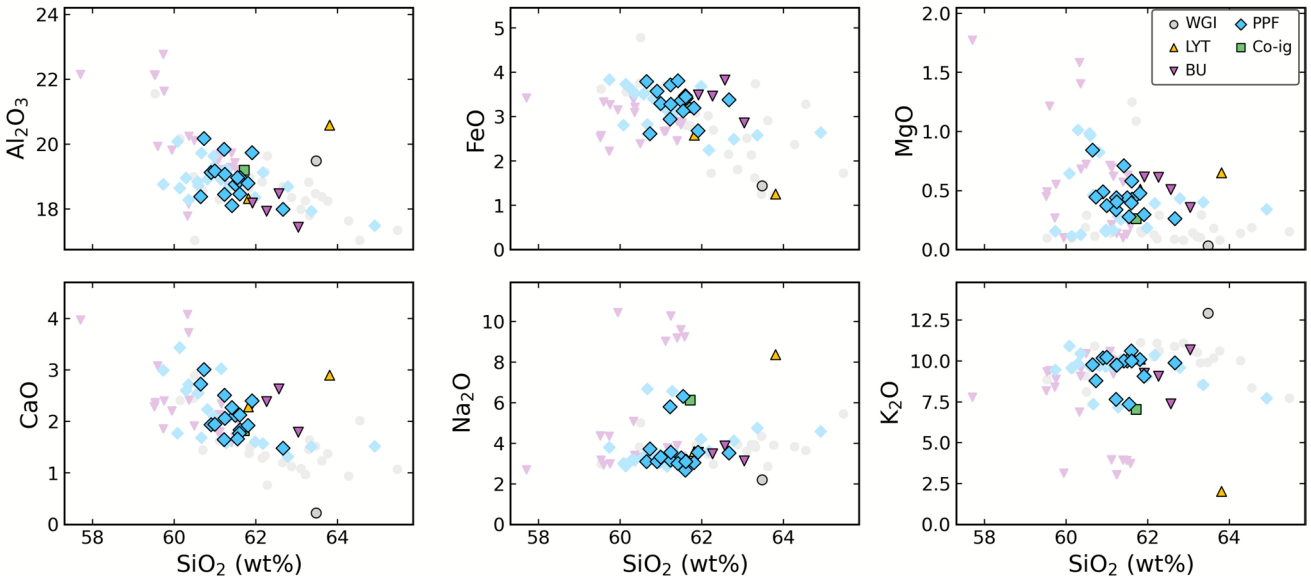

Fig. 3 Binary Harker diagrams for selected major oxides (wt%) as a function of SiO_2 concentrations in MI from this study (symbols with black outline) and the literature (faded symbols). Literature sources, unit symbols and colors are the same as in Fig. 2

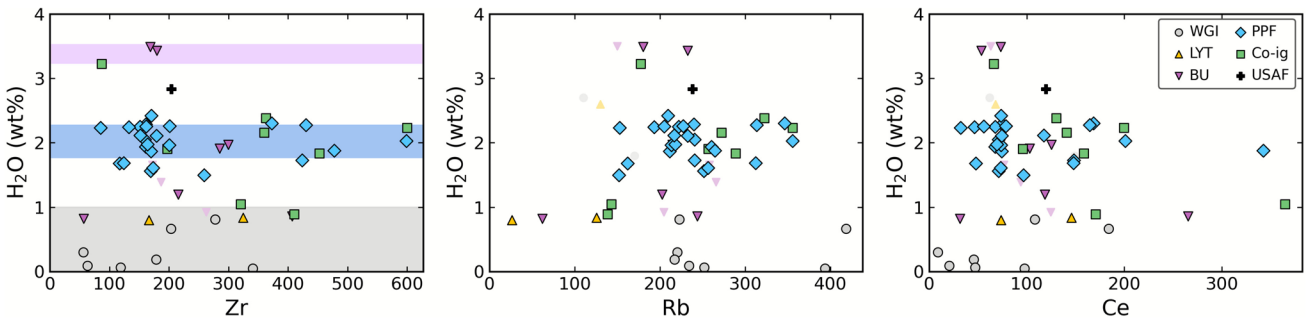

Fig. 4 Binary diagrams of H_2O as a function of Zr, Rb, and Ce (in ppm) in MI from this study (symbols with black outline) and the literature (faded symbols). Colored bands mark the low-H_2O (< 1 wt%, $n = 12$; gray), moderate-H_2O (2.02 ± 0.25 wt%, $n = 31$; blue), and high-H_2O (3.38 ± 0.14 wt%, $n = 3$; purple) groups discussed in the text. Literature sources, unit symbols and colors are the same as Fig. 2

WGI and LYT units contain MI with H_2O concentrations that are universally low, < 1 wt% ($n = 13$; Table 2, Fig. 4). MI H_2O concentrations in the PPF are consistent, averaging 2.01 ± 0.27 wt% H_2O ($n = 24$). BU MI are the most variable, ranging 0.8–3.46 wt% H_2O (1.95 ± 1.13, $n = 7$), which is most likely reflective of the nature of this unit as an amalgamation of multiple sources and possibly diverse emplacement temperatures. Co-ignimbrite fallout MI have a similarly wide range from 0.9–3.23 wt% (1.96 ± 0.75, $n = 7$), but this includes clear low-H_2O outliers at 0.9 and 1.0 wt% and one high-H_2O outlier at 3.23 wt%. Excluding low and high outliers, co-ignimbrite MI have H_2O concentrations matching those in the PPF at 2.10 ± 0.23 wt% ($n = 5$). The single MI from USAF has 2.84 wt% H_2O, just above the range of PPF and non-outlier co-ignimbrite MI but lower than the three MI with the highest H_2O contents (two BU and one co-ignimbrite MI; 3.38 ± 0.14, $n = 3$).

Chlorine concentrations vary widely across all units (Fig. S2). The lowest Cl concentrations are limited to slowly cooled units, generally < 2000 ppm with WGI largely near zero. PPF and co-ignimbrite MI show two distinct groups with Cl at ~ 4000 and ~ 8000 ppm. The majority of PPF MI cluster tightly at ~ 4000 ppm Cl with two PPF and all co-ignimbrite MI ~ 8000 ppm. Sulfur concentrations span the full range from < 50–1000 ppm for all units (Fig. S3). The PPF MI range from < 450–600 ppm S and correlate with FeO and MgO. Other units generally follow these trends with two clear outliers, one LYT and one WGI MI.

Magmatic temperatures and pressures

Equilibrium temperatures (T, °C) and saturation pressures (P, bar) were calculated using clinopyroxene-liquid thermobarometry (T) and H_2O-CO_2 solubility modeling (P) and are given in Supplementary Tables S2 and S3. Temperature calculations require a value for pressure as a model input and pressure calculations require a temperature value, so we performed modeling iteratively. For all samples, iterative calculation of temperature and pressure matched within 1% relative after one iteration.

All temperature calculations were performed using the Python3 program Thermobar (v1.0.60; Wieser et al. 2021) with the clinopyroxene-liquid geothermometer equations of Masotta et al. (2013), which is calibrated for use on alkaline samples. Model inputs are major oxide composition of the clinopyroxene and melt and pressure. Only nine MI have major element, H_2O, and host clinopyroxene compositions. Eight of nine MI have consistent temperatures of 930 ± 31 °C. The other MI is from the WGI unit and has a modeled temperature of 720 °C, which is anomalously low and does not agree with the range of published temperatures for the WGI (e.g., Fulignati et al. 2004; Marianelli et al. 2006; Severs 2007; Fowler et al. 2007; Masotta et al. 2013; Forni et al. 2016; Table S4). H_2O-CO_2 solubility has a minimal dependence of volatile solubility on temperature (Iacovino et al. 2021; Wieser et al. 2022), meaning our saturation pressure calculations are not meaningfully affected by our selection of temperature. We calculated saturation pressures using three temperatures for the entire dataset of 900, 950, and 1000 °C, which resulted in a $< 5\%$ relative decrease in pressure with increasing temperature for almost all samples (≤ 30 bar difference). The eight most H_2O-poor samples decreased $< 10\%$ relative, constituting a pressure difference of ≤ 10 bar.

Thermobar also evaluates whether clinopyroxene-melt pairs are in equilibrium using multiple criteria, including several published $K_D(Fe\text{-}Mg)_{cpx\text{-}melt}$ values, and quality of clinopyroxene analyses are evaluated based on measured Mg#, EnFs, DiHd, and CaTs. To assess the equilibrium of our clinopyroxene-MI pairs, we performed mineral-melt matching with Thermobar, which calculates all possible pairs for all clinopyroxenes against all glasses. Thirty-nine equilibrium pairs were found and produced modeled temperatures within ± 10 °C of 950 °C. Thus, we report results using a temperature of 950 °C.

Saturation pressures were calculated for each MI with the Python3 program VESIcal (v1.2.10; Iacovino et al. 2021) using the model of Ghiorso and Gualda (2015; "MagmaSat"). Model inputs are melt major oxide composition, H_2O and CO_2 concentrations, and temperature. The dependence of H_2O-CO_2 solubility on magma composition is only significant when compositions are considerably different (e.g., basalt vs rhyolite; Iacovino et al. 2021; Wieser et al. 2022). For samples that have measured H_2O concentrations but no EPMA, we use the average major element composition from other samples in the same unit for modeling purposes. CO_2 concentrations were not measured in MI in this study, but CO_2 solubilities are strongly dependent on pressure. Literature CO_2 concentrations are universally low, with values below 250 ppm (e.g., Severs 2007; Moretti et al. 2019). The majority of MI reported in the literature are below the detection limit of FTIR (~50 ppm; e.g., Signorelli et al. 1999; Marianelli et al. 2006). Pressures were calculated for all MI with CO_2 concentrations of 0, 50, and 250 ppm. From 0 to 50 ppm CO_2, pressures and depths increase by ~130% (1.3x) and from 50 to 250 ppm by ~200% (2x), on average. Campanian Ignimbrite MI with CO_2 concentrations > 50 ppm are rare, so we focus here only on our calculations with 50 ppm, which represent a reasonable maximum pre-eruption pressure. Using our sample groupings defined in Sect. "Volatile concentrations", low-H_2O samples have $P \leq 200$ bar, moderate-H_2O samples average 460 ± 72 bar, and high-H_2O samples average 920 ± 70 bar. Average major element compositions, H_2O concentrations, modeled storage pressures (and depths) are given in Table 3.

Pre-eruption magma storage depths

We can use our modeled saturation pressures for moderate- and high-H_2O MI to calculate the corresponding depth of MI storage within the crust just prior to eruption. We do not calculate pressures for low-H_2O MI since they experienced post-emplacement H^+ loss and do not represent pre-eruptive equilibrium H_2O concentrations.The pressure gradient of the crust in the region is not well constrained, with previous studies citing values that range between 150 and 270 bar/km (e.g., Fanara et al. 2015; Stock et al. 2018; Amstutz et al. 2025). Calculations over this range show a decrease in depth of 25% relative from 150 and 200 bar/km and 35% relative from 200 to 270 bar/km.

For this discussion, we use the middle pressure gradient of 200 bar/km and pressures calculated for MI with 50 ppm CO_2, which represent a reasonable maximum pressure for these MI, as discussed previously. Moderate-H_2O samples indicate a storage depth of 2.3 ± 0.36 km, and high-H_2O samples indicate a storage depth of 4.6 ± 0.35 km. All values are reported in Supplementary Table S2 and averages for each unit are given in Table 3.

Discussion

PDC deposits of the CI are typically several to tens of meters thick and, by analogy to other studied deposits including those of the nearby Vesuvius 79 CE eruption, cooled slowly (weeks to years; e.g., Giordano et al. 2018). H_2O concentrations measured in Welded Gray Ignimbrite (WGI) and

Lithified Yellow Tuff (LYT) MI are universally low (as low as 0.05 wt% and in all cases < 1 wt%), which would imply unreasonably shallow magma storage depths assuming saturation. PDC MI have a wide range in incompatible element concentrations (56–341 ppm Zr), reflecting fractionation processes inconsistent with these low H_2O values. Coupling this with the fact that these PDC units remained at temperatures > 580 °C during transport and emplacement (Cappelletti et al. 2003; Ort et al. 2018), we interpret that these MI lost H_2O via diffusive re-equilibration of hydrogen after emplacement (cf., Wallace 2001; Lloyd et al. 2013; Table S5). This interpretation is consistent with other studies of MI in ignimbrites (e.g., Lowenstern 2003), where MI are affected extensively by post-emplacement hydrogen loss, resulting in very low (< 1 wt%) H_2O concentrations. Three BU and two co-ignimbrite MI are also in the low-H_2O group (Table S2) and probably do not represent magmatic conditions. We interpret all samples in the low- and low-moderate-H_2O groups to be "degassed", meaning that hydrogen was diffusively lost from the MI to the surrounding deposit after emplacement.

For assessment of the pre-eruptive conditions of the CI magmas, we focus on MI in the moderate- and high-H_2O groups. This includes all Plinian Pumice Fall (PPF) MI, six of eight co-ignimbrite MI, and four BU MI. Given the lack of evidence for post-emplacement hydrogen loss coupled with melt compositions consistent with published values of unaltered melts, we consider the PPF a robust recorder of the conditions in the magma chamber just prior to eruption, consistent with a quickly cooled nature that typifies Plinian deposits.

The co-ignimbrite fallout was deposited concurrently with the WGI from the same PDC flow. Relatively high H_2O contents matching those of the PPF suggest they were not subjected to slow post-emplacement cooling like the massive PDC deposits. The PDCs flowed outward from the vent as dilute currents, with a denser lowermost section depositing the ignimbrite (Fisher et al. 1993; Scarpati et al. 2020). As the current lost solid material to sedimentation and expanded due to both magmatic gases exsolving from clasts and possible incorporation of air at its top, it became lighter and eventually ascended into the atmosphere to form a co-ignimbrite column, or "phoenix cloud" (e.g., Dobran et al. 1993; Silleni et al. 2024). This would mostly have happened at the farthest extent of its runout and possibly at the contact with the Apennine ridges (e.g. Calder et al. 1997; Dufek et al. 2015; Smith et al. 2016; Silleni et al. 2024). Silleni et al. (2020) estimate that the co-ignimbrite fallout is about the same volume as the ignimbrite, in agreement with numerical modeling of PDC/co-ignimbrite partitioning (Calabrò et al. 2022). The co-ignimbrite material deposited as cold fallout at more distal localities represents the material in the PDC but without H^+ loss from storage at high temperatures at surface pressures. There is a possibility that material deposited by the undercurrent in a PDC is weakly fractionated by density from the overriding current (which later becomes the co-ignimbrite plume), producing a small difference in the average composition of the two units (ignimbrite and co-ignimbrite). Both the host clinopyroxene composition and major and trace element compositions of the MI for the WGI and LYT overlap with the compositional range for the co-ignimbrite fallout. We therefore use co-ignimbrite fallout MI as a proxy for the magmatic conditions of the WGI and LYT. MI in the other fast-cooling units, such as the Unconsolidated Stratified Ash Flow (USAF), and portions of the Breccia Unit (BU), appear to have reliably maintained their H_2O concentrations after emplacement and show ranges of values similar to the co-ignimbrite fallout.

Evidence for saturation of CI magmas prior to eruption

Increases in incompatible trace element concentrations of MI with decreasing CaO and MgO (Table 2) are expected for a magma crystallizing clinopyroxene, and indicate the CI magma was undergoing crystallization and continuing to evolve throughout the period of MI entrapment. Zr behaves highly incompatibly in our MI, consistent with the lack of Zr-rich phases such as zircon in CI juvenile clasts, and comes from the same SIMS analyses as the H_2O data. We thus use increasing Zr melt concentration as a proxy for increasing extent of crystallization of a parent magma.

MI in the initial phase of the eruption (PPF) have a large range, 85–599 ppm, of Zr concentrations. These fall into two groups, with Zr = 85–259 and Zr = 373–599 ppm, implying that MI record either an evolving magma at various stages during that evolution or two magmas that were evolving in different reservoirs (Fig. 4). PPF H_2O concentrations remain consistent over this range with an average of 2.01 ± 0.27 wt% H_2O ($n = 24$), with no trend in H_2O with major or trace element concentrations (Fig. 4). The magma hosting PPF MI outgassed at a pressure in equilibrium with this water concentration (460 ± 77 bar). This could be due to either: 1) long-term magma storage and fractionation occurring at this depth or 2) deep, already-fractionated magma ascending to this depth during the runup to the eruption, at which time the MI outgassed during a brief shallow storage period.

Re-equilibration and shallow storage is best preserved in PPF MI but is not unique to this unit. The majority of MI in the co-ignimbrite fallout and Breccia Unit fall in the moderate-H_2O group. Altogether, moderate-H_2O MI concentrations of 2.02 ± 0.25 wt% ($n = 31$) imply storage, saturation, and re-equilibration at a similar pressure. We interpret moderate-H_2O MI as having a pre-eruptive pressure of 460 ± 72 bar, corresponding to a depth of 2.3 ± 0.36 km, which we term "shallow" magma storage.

The three MI with H_2O above 3 wt% (3.38 ± 0.14 wt%, $n = 3$; two BU and one co-ignimbrite) constitute a very small

dataset but nonetheless deserve discussion. Studies of volatiles in suites of MI often focus on those with the highest concentrations, particularly for H_2O since they represent the least degassed samples. If these are representative of real MI populations, they indicate a second, deeper storage region. We can then consider high-H_2O MI as having a pre-eruptive pressure of 920 ± 70 bar, corresponding to a depth of 4.6 ± 0.35 km, which we term "deep" magma storage.

Simultaneous tapping of magma lenses at different depths was proposed by Cashman and Giordano (2014) as an alternative model to the classic withdrawal from a single zoned magma chamber. Either model may apply to the CI eruption although the roof of a sill complex may be more stable than a large chamber at very shallow depths. Opening of new vents and increased magma eruption rate during a caldera collapse could allow magmas to be sourced from deeper in the magmatic system, allowing for sampling of MI in equilibrium with magmas of higher H_2O saturation limits.

Timescales of pre-eruptive magma storage

Long-term storage of a hot magma body large enough to feed the CI at a depth of 2.3 km is difficult to explain given the potential geophysical instabilities this may pose. Voluminous silicic magma bodies are commonly interpreted to have "shallow storage" zones between 4–10 km (Wilson et al. 2021). Long-term shallow storage of CI magmas at only 2.3 km is unlikely given the increased propensity for roof collapse during the storage period. We instead favor a hypothesis in which deep fractionated magma ascended to 2.3 km for a short pre-eruptive period. In this model, the magma producing the PPF was briefly stored at a shallow pressure (460 ± 72 bar), with MI H_2O concentrations re-equilibrating to the H_2O saturation limit (2.02 ± 0.25 wt%) prior to eruption (Fig. 5). Therefore, moderate-H_2O MI do not record the full magmatic volatile history in the CI but, rather, conditions during a short-lived, shallow storage event during which re-equilibration allowed hydrogen to escape from the MI while water exsolved from the magma. We modeled the hydrogen diffusion timescales in a Monte Carlo simulation over a conservative range of values to obtain the "worst case" scenario; i.e., where the minimum time required for MI to completely re-equilibrate is the longest. Modeling results indicate that a pre-eruptive storage period as brief as 2–15 days prior to eruption is amply sufficient to totally reset MI H_2O concentrations (see Supplementary Material; Fig. S5; Table S5). Major and trace elements were not affected by this re-equilibration, as their diffusion rates are extremely slow by comparison (e.g., Cherniak and Dimanov 2010; Zhang et al. 2010), and so MI maintain the concentrations of those elements from the original conditions of entrapment. The Cl and S concentrations in MI from the slowly cooled deposits are significantly lower than those in the quickly cooled units, which may indicate that they diffuse on

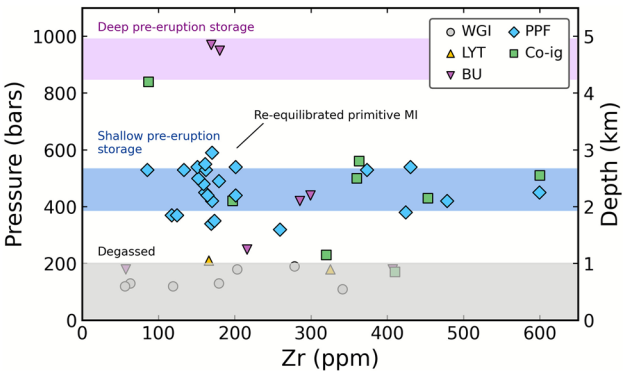

Fig. 5 Calculated equilibration pressures in bar assuming 50 ppm CO_2 in MI (left y-axis) and corresponding depth estimates assuming a 200 bar/km pressure gradient (right y-axis) as a function of Zr concentration (x-axis) in melt inclusions from this study (symbols with black outline) and the literature (faded symbols). Literature sources, unit symbols and colors are the same as in Fig. 2. MI in the high-H_2O group (3.38 ± 0.14 wt%, $n = 3$; two BU and one co-ignimbrite; purple band) correspond to an equilibration depth of 4.6 ± 0.35 km (920 bar) representing a region of "deep" pre-eruption storage and potentially a reservoir where the two CI magma types exchanged crystal cargo. All PPF and most co-ig MI, which are the fastest cooled units sampled, plus two BU MI are in the moderate-H_2O group and contain 2.02 ± 0.25 wt% H_2O (n = 31; blue band) corresponding to an equilibration depth of 2.3 ± 0.36 km (460 bar). In this region, primitive and evolved MI from both CI magma types are represented by trace and major element concentrations, suggesting crystal exchange between the two magmas at a deeper region followed by a brief period of magma storage at 2.3 km, during which H_2O concentrations were "reset" to a consistent ~ 2 wt% via diffusive reequilibration. MI below 200 bar (1 km; gray bar) are considered degassed, consistent with slowly cooled units plotting exclusively in this region

the time scales of cooling of the CI (minimum times on the order of 0.5–5 years based on hydrogen diffusion modeling).

Eruption dynamics

Two distinct melts fed the CI eruption, one relatively primitive and the other relatively evolved (e.g., Smith et al. 2016). Matrix glass compositions in the first Plinian phase of the eruption (PPF) all correspond to the most evolved melt (Tomlinson et al. 2012; Smith et al. 2016; Gallo et al. 2024). MI in PPF crystals, however, record both melts (Figs. 3, 4), suggesting crystal exchange between the two magmas prior to shallow storage at 2.3 km. A large amount of space must have been made in the crust to account for the proposed shallow storage and re-equilibration of magmas supplying the CI eruption. The eruptive volume of the Plinian Pumice Fallout alone is estimated to be 2–22 km^3 DRE (Rosi et al. 1999; Marti et al. 2016; Silleni et al. 2020), with the volume of the remaining units estimated at ~ 181–265 km^3 DRE (Silleni et al. 2020).

Our model for CI magmatic system starts with storage of least evolved magma (Zr < 300 ppm) and entrapment of

H_2O-rich melt inclusions (6 wt%; Marianelli et al. 2006) at ~ 9 km depth (Fig. 6), followed by migration of the magma to 4.6 ± 0.35 km (~ 3.4 wt% H_2O; ~ 920 bar) with concomitant differentiation of magma in discrete sills (Fig. 6), similar to the model of Cashman and Giordano (2014). The first erupted unit, the Plinian Pumice Fallout (PPF), is entirely sourced from the evolved melt, as indicated by matrix glass compositions. MI in PPF clinopyroxene crystals, however, contain both primitive and evolved glass compositions, indicating crystal exchange between the two melts. Because all PPF MI have H_2O contents of ~ 2 wt%, we suggest that further magma ascent and shallow storage of evolved magma at 2.3 ± 0.25 km depth (~ 2 wt% H_2O; ~ 460 bar) occurred after differentiation and crystal exchange and just prior to eruption. The consistent H_2O contents across MI glass compositions were caused by re-equilibration of MI H_2O contents via hydrogen diffusion over 1–2 weeks time period. The Breccia Unit erupted during caldera collapse over a geographically large range of vents, sampling magma sourced from all magma storage depths in the overall eruption (Fig. 6). Some parts of the Breccia Unit cooled quickly, perhaps due to incorporation of cold breccia clasts.

Magma sills may have extended laterally beneath the entire caldera and probably outside the caldera boundaries. Eruption from laterally extensive discrete sills could account for the localized spatter deposits observed a few kilometers outside the caldera limits, such as at San Martino and on the island of Procida (Fedele et al. 2008; Orsi 2022). Storage and brief re-equilibration of magmas in discrete sills in the shallow crust explains the limited range in water concentrations with a wider range in incompatible element concentrations in MI. Growth of a large contiguous magma body to such shallow depths would require a gradually thinning roof. Rapid intrusion of a sill, followed quickly by eruption days to weeks later, would allow for magma re-equilibration and magma outgassing but not require a thin roof to be stable over a long period. Additionally, the presence of multiple separate magma bodies beneath Campi Flegrei and possible associated pre-eruptive tumescence could explain the limited caldera subsidence associated with the eruption of the CI (De Natale et al. 2016). Defining a specific geometry of storage conditions is beyond the scope of our current knowledge.

It is uncertain what the H_2O concentrations of these MI were at the time of entrapment since all of the MI in this study show evidence of re-equilibration. Marianelli et al. (2006) report MI with up to 6 wt% H_2O in the CI, which we suspect represent batches of magma that came up quickly to feed the eruption but were not found in the samples we studied. This can be envisaged as a possible starting concentration, which implies that up to 4 wt% H_2O of excess vapor phase could have been lost via re-equilibration just prior to eruption. Exsolution of H_2O from the magma may have occurred within a two-week period, but the gas could take longer than this to escape the entire system. If present at the time of eruption, an excess 4 wt% H_2O in the vapor phase would have supplied abundant hot gas at the eruption onset, providing the driving force for the gas-rich, expanded PDC.

Comparison to later eruptions of Campi Flegrei

The CI eruption was the first known caldera-forming eruption of Campi Flegrei and the volcanic field remains active today. The proposed geometry of shallow sills and re-equilibration of magmas supplying the CI eruption is a larger scale version of proposed mechanisms for more recent small eruptions from vents within the caldera (e.g., Stock et al. 2016, 2018). Eight eruptions in Campi Flegrei from the past 15 kyr have been investigated via MI and apatite crystals for volatile concentrations (Stock et al. 2016, 2018). MI studied in the < 15 kyr eruptions typically contain ~ 2–4 wt% H_2O, similar to the H_2O concentrations in this study (Stock et al. 2016, 2018). Stock et al. (2016) proposed that the young MI were affected by extensive hydrogen diffusion after entrapment, resetting H_2O contents. This is the same mechanism proposed in this study, but the CI re-equilibration and storage occurred simultaneously on a much larger scale.

Analysis of apatite crystals from the < 15-ka Campi Flegrei deposits suggest the melts that fed those eruptions underwent shallow storage and late-stage volatile saturation. Two trends in volatile compositions of apatite crystals were observed, one belonging to conditions of volatile-undersaturated crystallization and one of volatile-saturated crystallization (Stock et al. 2016, 2018). For the CI magmas, there is evidence for volatile undersaturation (e.g., Fanara et al. 2015) earlier in the magmatic history than what the MI in this study record, with shallow storage and volatile saturation occurring close to the time of eruption. We propose that the same processes are at play with both small and large eruptions in Campi Flegrei. Magmas are volatile undersaturated, then move to shallow storage in which re-equilibration and volatile saturation occur, and the eruption commences shortly after reaching volatile saturation.

Calculated depths of 2–3 km for the Campanian Ignimbrite and the < 15 kyr eruptions (Stock et al. 2016, 2018; Amstutz et al. 2025) are similar to the depth of recent sill emplacement in Campi Flegrei (e.g., Zollo et al. 2008; De Siena et al. 2010; Isaia et al. 2025). This suggests that these processes may have been, and continue to be, important in the Campi Flegrei system.

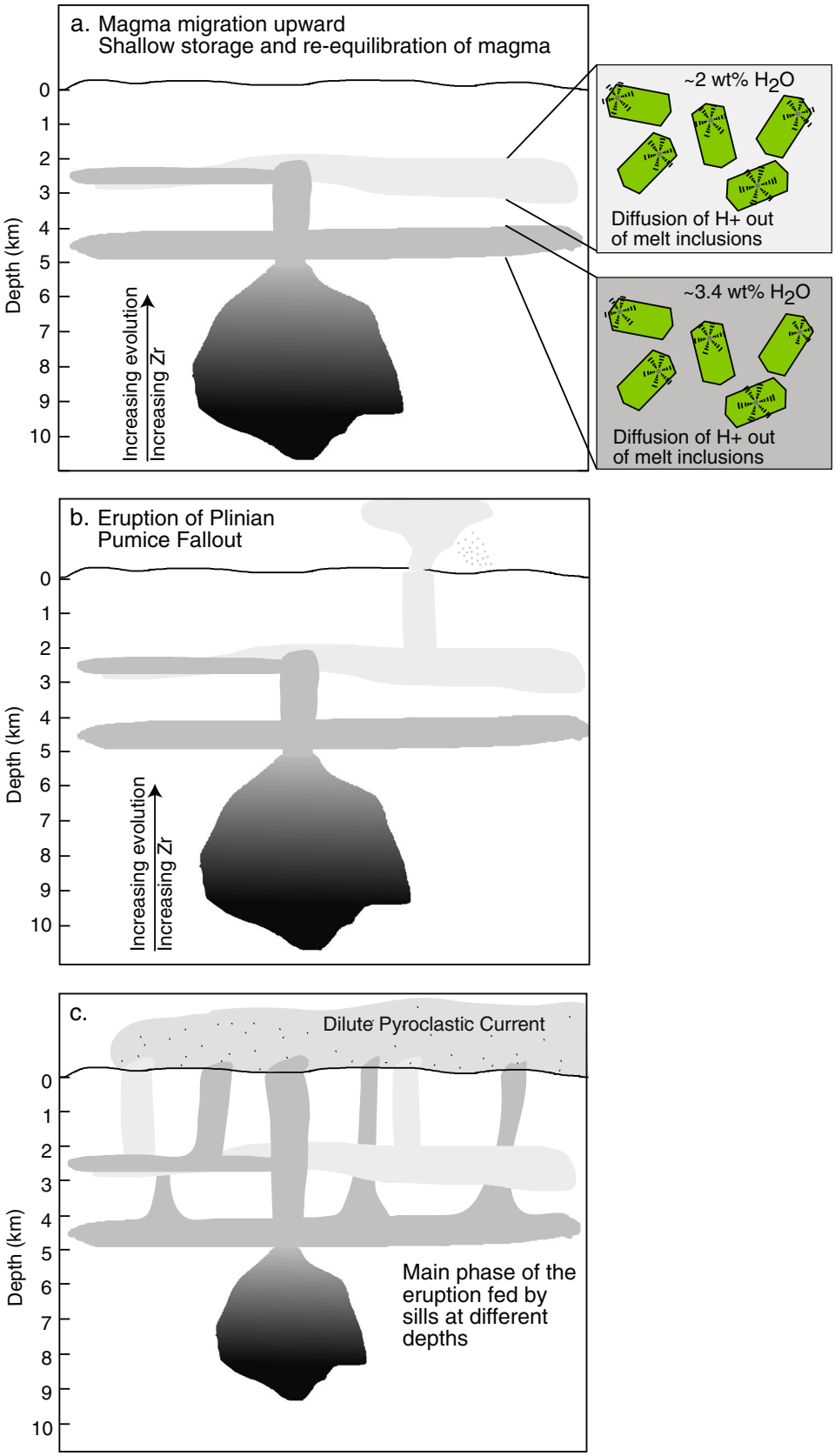

Fig. 6 Illustrative sketches showing the proposed model for the plumbing system that fed the Campanian Ignimbrite. (**a**) Magma migration into sills at shallow levels (~2-5 km) from the deeper system, which is inferred by the H_2O-rich (~6 wt%) melt inclusions reported by Marianelli et al. (2006), that correspond to a depth of ~9 km. The uppermost, most evolved magma, as indicated by lighter coloration, is shallowly stored (~2.3 km) and allows re-equilibration via hydrogen diffusion of melt inclusions to ~2 wt% H_2O. A less evolved magma, as indicated by darker coloration, is stored at greater depth (~4.6 km), and melt inclusions re-equilibrate via hydrogen diffusion to ~3.4 wt% H_2O as the magma stalls on the way to the surface. (**b**) Eruption of Plinian Pumice Fallout, resulting in deposits with melt inclusions containing ~2 wt% H_2O. (**c**) Eruption of the less evolved CI magma, which erupts along with the other melt, producing PDCs and co-ignimbrite fallout. These erupted magmas are sourced from sills at various depths, evidenced by a range of melt inclusion H_2O concentrations. Deeper storage and faster rates of discharge allow for higher H_2O and lower zirconium concentration

Conclusions

The first phase of the CI eruption was fed by magma that was stored shallowly for up to 2 weeks prior to eruption. During this shallow storage, re-equilibration of magmatic water concentrations occurred, as testified by the recognition of two groups of clinopyroxene-hosted MI: a moderate-H_2O group with 2.02 ± 0.25 wt% H_2O ($n = 31$) correlating to shallow storage at 2.3 ± 0.36 km (460 ± 72 bar); and a high-H_2O group with 3.38 ± 0.14 wt% H_2O, correlating to deep storage at 4.6 ± 0.4 km (920 ± 70 bar). The highest published H_2O concentration in these units is 6 wt% (Marianelli et al. 2006), suggesting that as much as ~ 4 wt% H_2O was lost during shallow storage and re-equilibration. If the excess fluid did not escape the magmatic system (to the surface or wall-rocks), it may have provided a gas source for the immediate expansion of PDCs emplacing the CI deposits.

Previous models of the CI magma system envisaged the storage system as deep (7–9 km) in large pods (Arienzo et al. 2009, 2011), consistent with what we model as the notional parent magma recorded by MI with 6 wt% H_2O (Marianelli et al. 2006). However, with evidence of shallow storage, the immediately pre-eruptive CI magmatic system can now be envisaged as a vertically extensive storage system with sills at multiple levels.

Supplementary Information The online version contains supplementary material available at https://doi.org/10.1007/s00445-026-01938-0.

Acknowledgements We thank Richard Hervig for his assistance with the Secondary Ion Mass Spectrometer, and Lynda Williams, Maitrayee Bose, Brendan Chapman, and Mara Karageozian for assistance with use of the indium mounting facilities and preparation of samples for SIMS. Comments by Lorenzo Fedele and an anonymous reviewer greatly improved the manuscript. Editorial care by Alexei Ivanov, Marie Edmonds, and Richard Herd is gratefully acknowledged.

Author contribution Allyson N. Murray: Investigation, Methodology, Data Collection, Formal analysis, Visualization, Writing – original draft, Writing – review & editing. Michael H. Ort: Conceptualisation, Investigation, Methodology, Resources, Formal analysis, Funding acquisition, Supervision, Writing – review & editing, Project administration. Kayla Iacovino: Conceptualisation, Investigation, Methodology, Visualization, Data Curation, Formal Analysis, Writing – review & editing. Victoria C. Smith: Conceptualisation, Investigation, Data Collection, Resources, Formal analysis, Funding acquisition, Writing – review & editing. Guido Giordano: Conceptualisation, Investigation, Resources, Funding acquisition, Writing – review & editing. Roberto Isaia: Conceptualisation, Investigation, Resources, Funding acquisition, Writing – review & editing.

Funding Funding for this project was provided by NSF grant EAR1761713 to MHO and NERC grant NE/5003584/1 to VCS. KI was supported by the NASA Jacobs JETS contract #NNJ13HA01C. GG acknowledges the grant to the Department of Science, Roma Tre University (MIUR–Italy Dipartimenti di Eccellenza, ARTICOLO 1, COMMI314–337 LEGGE 232/2016). ANM was also supported by the Tom and Rose Bedwell Earth Physics Award, Pioneer Natural Resources, and the Friday Lunch Clubbe.

Data availability All data presented in supplemental material.

Declarations

Competing interests The authors declare no competing interests.

References

Amstutz FM, Stock MJ, Smith VC, Isaia R, Vitale S, Carter EJ, Natale J (2025) Volcano-tectonic controls on magmatic evolution at Campi Flegrei, Italy: insights from thermodynamic modelling. J Petrol 66:egaf068. https://doi.org/10.1093/petrology/egaf068

Anderson AT (1974) Chlorine, sulfur, and water in magmas and oceans. Geol Soc Am Bull 85:1485–1492

Anderson AT (1979) Water in some hypersthenic magmas. J Geol 87:509–531

Anikovich MV, Sinitsyn AA, Hoffecker JF, Holliday VT, Popov VV, Lisitsyn SN, Forman SL, Levkovskaya GM, Pospelova GA, Kuz'mina IE, Burova ND, Goldberg P, Macphail RI, Giaccio B, Praslov ND (2007) Early upper Paleolithic in eastern Europe and implications for the dispersal of modern humans. Science 315:223–226. https://doi.org/10.1126/science.1133376

Arienzo I, Civetta L, Heumann A, Wörner G, Orsi G (2009) Isotopic evidence for open system processes within the Campanian Ignimbrite (Campi Flegrei-Italy) magma chamber. Bull Volcanol 71:285–300. https://doi.org/10.1007/s00445-008-0223-0

Arienzo I, Heumann A, Wörner G, Civetta L, Orsi G (2011) Processes and timescales of magma evolution prior to the Campanian Ignimbrite eruption (Campi Flegrei, Italy). Earth Planet Sci Lett 306:217–228. https://doi.org/10.1016/j.epsl.2011.04.002

Barberi F, Innocenti F, Lirer L, Munno R, Pescatore TS, Santacroce R (1978) The Campanian Ignimbrite: a major prehistoric eruption in the Neapolitan area (Italy). Bull Volcanol 41:10–31. https://doi.org/10.1007/bf02597680

Blake S (1984) Volatile oversaturation during the evolution of silicic magma chambers as an eruption trigger. J Geophys Res Solid Earth 89:8237–8244. https://doi.org/10.1029/jb089ib10p08237

Calabrò L, Esposti Ongaro T, Giordano G, de' Michieli Vitturi M (2022) Reconstructing pyroclastic currents' source and flow parameters from deposit characteristics and numerical modeling: the Pozzolane Rosse Ignimbrite case study (Colli Albani, Italy). J Geophys Res Solid Earth 127:1–26. https://doi.org/10.1029/2021JB023637

Calder ES, Sparks RSJ, Woods AW (1997) Dynamics of co-ignimbrite plumes generated from pyroclastic flows of Mount St. Helens (7 august 1980). Bull Volcanol 58:432–440

Cappelletti P, Cerri G, Colella A, de' Gennaro M, Langella A, Perrotta A, Scarpati C (2003) Post-eruptive processes in the Campanian Ignimbrite. Mineral Petrol 79:79–97. https://doi.org/10.1007/s00710-003-0003-7

Cashman KV, Giordano G (2014) Calderas and magma reservoirs. J Volcanol Geotherm Res 288:28–45. https://doi.org/10.1016/j.jvolgeores.2014.09.007

Cherniak DJ, Dimanov A (2010) Diffusion in pyroxene, mica and amphibole. Rev Mineral Geochem 72:641–690. https://doi.org/10.2138/rmg.2010.72.14

Civetta L, Orsi G, Pappalardo L, Fisher RV, Heiken G, Ort M (1997) Geochemical zoning, mingling, eruptive dynamics and depositional processes - the Campanian Ignimbrite, Campi Flegrei caldera, Italy. J Volcanol Geotherm Res 75:183–219. https://doi.org/10.1016/S0377-0273(96)00027-3

Costa A, Folch A, Macedonio G, Giaccio B, Isaia R, Smith VC (2012) Quantifying volcanic ash dispersal and impact of the Campanian ignimbrite super-eruption. Geophys Res Lett. https://doi.org/10.1029/2012gl051605

De Natale G, Troise C, Mark D, Mormone A, Piochi M, Di Vito MA, Isaia R, Carlino S, Barra D, Somma R (2016) The Campi Flegrei deep drilling project (CFDDP): new insight on caldera structure, evolution and hazard implications for the Naples area (Southern Italy). Geochem Geophys Geosyst 17:4836–4847. https://doi.org/10.1029/2017GC007297

De Siena L, Del Pezzo E, Bianco F (2010) Seismic attenuation imaging of Campi Flegrei: evidence of gas reservoirs, hydrothermal basins, and feeding systems. J Geophys Res Solid Earth. https://doi.org/10.1029/2009JB006938

Di Salvo S, Avanzinelli R, Isaia R, Zanetti A, Druitt T, Francalanci L (2020) Crystal-mush reactivation by magma recharge: evidence from the Campanian Ignimbrite activity, Campi Flegrei volcanic field, Italy. Lithos 376:105780. https://doi.org/10.1016/j.lithos.2020.105780

Dobran F, Neri A, Macedonio G (1993) Numerical simulation of collapsing volcanic columns. J Geophys Res 98:4231–4259. https://doi.org/10.1029/92JB02409

Dufek J, Esposti Ongaro T, Roche O (2015) Chapter 35: Pyroclastic density currents: Processes and models. In: Sigurdsson H (ed) Encyclopedia of Volcanoes, second edition. Academic Press, pp 617–629

Engwell SL, Sparks RS, Carey S (2014) Physical characteristics of tephra layers in the deep sea realm: the Campanian Ignimbrite eruption. Geol Soc Lond Spec Publ 398:47–64. https://doi.org/10.1144/sp398.7

Fanara S, Botcharnikov RE, Palladino DM, Adams F, Buddensieck J, Mulch A, Behrens H (2015) Volatiles in magmas related to the Campanian Ignimbrite eruption: experiments vs. natural findings. Am Mineral 100:2284–2297. https://doi.org/10.2138/am-2015-5033

Fedele L, Scarpati C, Lanphere M, Melluso L, Morra V, Perrotta A, Ricci G (2008) The Breccia Museo formation, Campi Flegrei, southern Italy: geochronology, chemostratigraphy and relationship with the Campanian Ignimbrite eruption. Bull Volcanol 70:1189–1219. https://doi.org/10.1007/s00445-008-0197-y

Fedele L, Scarpati C, Sparice D, Perrotta A, Laiena F (2016) A chemostratigraphic study of the Campanian Ignimbrite eruption (Campi Flegrei, Italy): insights on magma chamber withdrawal and deposit accumulation as revealed by compositionally zoned stratigraphic and facies framework. J Volcanol Geotherm Res 324:105–117. https://doi.org/10.1016/j.jvolgeores.2016.05.019

Fisher RV, Orsi G, Ort M, Heiken G (1993) Mobility of a large-volume pyroclastic flow - emplacement of the Campanian Ignimbrite, Italy. J Volcanol Geotherm Res 56:205–220. https://doi.org/10.1016/0377-0273(93)90017-L

Forni F, Bachmann O, Mollo S, De Astis G, Gelman SE, Ellis BS (2016) The origin of a zoned ignimbrite: insights into the Campanian Ignimbrite magma chamber (Campi Flegrei, Italy). Earth Planet Sci Lett 449:259–271. https://doi.org/10.1016/j.epsl.2016.06.003

Forni F, Degruyter W, Bachmann O, Mollo S, De Astis G, Piochi M (2018) Long-term magmatic evolution reveals the beginning of a new caldera cycle at Campi Flegrei. Sci Adv 4. https://doi.org/10.1126/sciadv.aat9401

Fowler SJ, Spera FJ, Bohrson WA, Belkin HE, De Vivo B (2007) Phase equilibria constraints on the chemical and physical evolution of the Campanian Ignimbrite. J Petrol 48:459–493. https://doi.org/10.1093/petrology/egl068

Fulignati P, Marianelli P, Proto M, Sbrana A (2004) Evidences for disruption of a crystallizing front in a magma chamber during caldera collapse: an example from the Breccia Museo unit (Campanian Ignimbrite eruption, Italy). J Volcanol Geotherm Res 133:141–155. https://doi.org/10.1016/S0377-0273(03)00395-0

Gallo RI, Ort MH, Iacovino K, Silleni A, Smith VC, Giordano G, Isaia R, Boro J (2024) Reconciling complex stratigraphic frameworks reveals temporally and geographically variable depositional patterns of the Campanian Ignimbrite. Geosphere 20(1):1–22. https://doi.org/10.1130/GES02651.1

Ghiorso MS, Gualda GAR (2015) An H_2O–CO_2 mixed fluid saturation model compatible with rhyolite-MELTS. Contrib Mineral Petrol 169:1–30. https://doi.org/10.1007/s00410-015-1141-8

Giaccio B, Isaia R, Fedele FG, Di Canzio E, Hoffecker J, Ronchitelli A, Sinitsyn AA, Anikovich M, Lisitsyn SN, Popov VV (2008) The Campanian ignimbrite and Codola tephra layers: two temporal/stratigraphic markers for the Early Upper Palaeolithic in southern Italy and eastern Europe. J Volcanol Geotherm Res 177:208–226. https://doi.org/10.1016/j.jvolgeores.2007.10.007

Giaccio B, Hajdas I, Isaia R, Deino A, Nomade S (2017) High-precision ^{14}C and $^{40}Ar/^{39}Ar$ dating of the Campanian Ignimbrite (Y-5) reconciles the time-scales of climatic-cultural processes at 40 ka. Sci Rep 7:1–10. https://doi.org/10.1038/srep45940

Giordano G, Zanella E, Trolese M, Baffioni C, Vona A, Caricchic C, DeBenedetti AA, Corrado A, Romano C, Sulpizio R, Geshi N (2018) Thermal interactions of the AD79 Vesuvius pyroclastic density currents and their deposits at Villa dei Papiri (Herculaneum archaeological site, Italy). Earth Planet Sci Lett 490:180–192. https://doi.org/10.1016/j.epsl.2018.03.023

Hervig RL, Mazdab FK, Moore G, McMillan PF (2003) Analyzing hydrogen (H_2O) in silicate glass by secondary ion mass spectrometry and reflectance Fourier transform infrared spectroscopy. Dev Volcanol, Elsevier 5:83–103

Iacovino K, Ju-Song K, Sisson T, Lowenstern J, Ri KH, Jang JN, Song KH, Ham SH, Oppenheimer C, Hammond JOS, Donovan A, Liu KW, Ryu KR (2016) Quantifying gas emissions from the "millennium eruption" of Paektu volcano, Democratic People's Republic of Korea/China. Sci Adv 2:1–12. https://doi.org/10.1126/sciadv.1600913

Iacovino K, Matthews S, Wieser PE, Moore GM, Bégué F (2021) VESIcal part I: an open-source thermodynamic model engine for mixed volatile (H_2O-CO_2) solubility in silicate melts. Earth Space Sci 8:1–55. https://doi.org/10.1029/2020EA001584

Isaia R, Troiano A, Giuseppe MGD, Paola CD, Gottsmann J, Pagliara F, Smith VC, Stock MJ (2025) 3D magnetotelluric imaging of a transcrustal magma system beneath the Campi Flegrei caldera, southern Italy. Commun Earth Environ 6:213. https://doi.org/10.1038/s43247-025-02185-5

Koyaguchi T, Suzuki YJ, Takeda K, Inagawa S (2018) The condition of eruption column collapse: 2. Three-dimensional numerical simulations of eruption column dynamics. J Geophys Res Solid Earth 123:7483–7508. https://doi.org/10.1029/2017JB015259

Le Maitre RW, Streckeisen A, Zanettin B, Le Bas MJ, Bonin B, Bateman P, Bellieni G, Dudek A, Efremova S, Keller J, Lameyre J, Sabine PA, Schmid R, Sorenson H, Wooley AR (2002) Igneous

rocks. A classification and glossary of terms; Cambridge University Press, Cambridge, p 236
Lloyd AS, Plank T, Ruprecht P, Hauri EH, Rose W (2013) Volatile loss from melt inclusions in pyroclasts of differing sizes. Contrib Mineral Petrol 165:129–153. https://doi.org/10.1007/s00410-012-0800-2
Lowenstern JB (1995) Applications of silicate-melt inclusions to the study of magmatic volatiles. In Thompson JFH, Magmas, fluids and ore deposits. Mineral Assoc Canada Short Course 23:71–99
Lowenstern JB (2003) Melt inclusions come of age: volatiles, volcanoes, and Sorby's legacy. Dev Volcanol 5:1–21. https://doi.org/10.1016/S1871-644X(03)80021-9
Marianelli P, Sbrana A, Proto M (2006) Magma chamber of the Campi Flegrei supervolcano at the time of eruption of the Campanian Ignimbrite. Geology 34:937–940. https://doi.org/10.1130/G22807A.1
Marti A, Folch A, Costa A, Engwell S (2016) Reconstructing the Plinian and co-ignimbrite sources of large volcanic eruptions: a novel approach for the Campanian Ignimbrite. Sci Rep 6:21220. https://doi.org/10.1038/srep21220
Masotta M, Mollo S, Freda C, Gaeta M, Moore G (2013) Clinopyroxene-liquid thermometers and barometers specific to alkaline differentiated magmas. Contrib Mineral Petrol 166:1545–1561. https://doi.org/10.1007/s00410-013-0927-9
Melluso L, Morra V, Perrotta A, Scarpati C, Adabbo M (1995) The eruption of the Breccia Museo (Campi Flegrei, Italy): fractional crystallization processes in a shallow, zoned magma chamber and implications for the eruptive dynamics. J Volcanol Geotherm Res 68:325–339
Moretti R, Arienzo I, Di Renzo V, Orsi G, Arzilli F, Brun F, D'Antonio M, Mancini L, Deloule E (2019) Volatile segregation and generation of highly vesiculated explosive magmas by volatile-melt fining processes: the case of the Campanian Ignimbrite eruption. Chem Geol 503:1–14. https://doi.org/10.1016/j.chemgeo.2018.10.001
Orsi G (2022) Volcanic and deformation history of the Campi Flegrei volcanic field, Italy. In: Orsi G, D'Antonio M, Civetta L (eds) Campi Flegrei: A restless caldera in a densely populated area. Springer Berlin, pp 1–53. https://doi.org/10.1007/978-3-642-37060-1_1
Ort MH, Orsi G, Pappalardo L, Fisher RV (2003) Anisotropy of magnetic susceptibility studies of depositional processes in the Campanian Ignimbrite, Italy. Bull Volcanol 65:55–72
Ort M, Giordano G, Zanella E, Isaia R, Silleni A, Smith VC (2018) Supercharging a pyroclastic density current with caldera hydrothermal fluids: Campanian Ignimbrite, Italy. Cities on Volcanoes Conference, Naples, Abst 513:01.17, p 411. https://editoria.ingv.it/miscellanea/2018/miscellanea43/#
Pappalardo L, Civetta L, D'Antonio M, Deino A, Vito MD, Orsi G, Carandente A, Vita SD, Isaia R, Piochi M (1999) Chemical and Sr-isotopical evolution of the Phlegraean magmatic system before the Campanian Ignimbrite and the Neapolitan Yellow Tuff eruptions. J Volcanol Geotherm Res 91:141–166. https://doi.org/10.1016/S0377-0273(99)00033-5
Pappalardo L, Piochi M, D'Antonio M, Civetta L, Petrinit R (2002a) Evidence for multi-stage magmatic evolution during the past 60 kyr at Campi Flegrei (Italy) deduced from Sr, Nd and Pb isotope data. J Pet 43:1415–1434. https://doi.org/10.1093/petrology/43.8.1415
Pappalardo L, Civetta L, De Vita S, Di Vito M, Orsi G, Carandente A, Fisher RV (2002b) Timing of magma extraction during the Campanian Ignimbrite eruption (Campi Flegrei Caldera). J Volcanol Geotherm Res 114:479–497. https://doi.org/10.1016/S0377-0273(01)00302-X
Parfitt EA, Wilson L (2008) Fundamentals of physical volcanology. Blackwell, Oxford
Pyle DM, Ricketts GD, Margari V, van Andel TH, Sinitsyn AA, Praslov ND, Lisitsyn S (2006) Wide dispersal and deposition of distal tephra during the Pleistocene 'Campanian Ignimbrite/Y5' eruption, Italy. Quat Sci Rev 25:2713–2728. https://doi.org/10.1016/j.quascirev.2006.06.008
Rosi M, Vezzoli L, Aleotti P, Censi MD (1996) Interaction between caldera collapse and eruptive dynamics during the Campanian Ignimbrite eruption, Phlegraean Fields. Ital. Bull Volcanol 57:541. https://doi.org/10.1007/s004450050111
Rosi M, Vezzoli L, Castelmenzano A, Grieco G (1999) Plinian pumice fall deposit of the Campanian ignimbrite eruption (Phlegraean Fields, Italy). J Volcanol Geotherm Res 91:179–198. https://doi.org/10.1016/s0377-0273(99)00035-9
Scarpati C, Sparice D, Perrotta A (2015) The ground layer of the Campanian ignimbrite: an example of deposition from a dilute pyroclastic density current. Bull Volcanol 77:97. https://doi.org/10.1007/s00445-015-0985-0
Scarpati C, Sparice D, Perrotta A (2020) Dynamics of large pyroclastic currents inferred by the internal architecture of the Campanian Ignimbrite. Sci Rep 10:1–13. https://doi.org/10.1038/s41598-020-79164-7
Severs MJ (2007) Applications of melt inclusions to problems in igneous petrogenesis. PhD thesis, Virginia Polytechnic Institute and State University. https://vtechworks.lib.vt.edu/server/api/core/bitstreams/988045ae-8eab-439f-be9b-59ee2f79a7cc/content
Signorelli S, Vaggelli G, Francalanci L, Rosi M (1999) Origin of magmas feeding the Plinian phase of the Campanian Ignimbrite eruption, Phlegrean Fields (Italy): constraints based on matrix-glass and glass-inclusion compositions. J Volcanol Geotherm Res 91:199–220. https://doi.org/10.1016/S0377-0273(99)00036-0
Signorelli S, Vaggelli G, Romano C, Carroll MR (2001) Volatile element zonation in Campanian Ignimbrite magmas (Phlegrean Fields, Italy): evidence from the study of glass inclusions and matrix glasses. Contrib Mineral Petrol 140:543–553. https://doi.org/10.1007/s004100000213
Silleni A (2019) Magnitude, transport and deposition of the 40-ka large-volume Campanian Ignimbrite. PhD dissertation, Roma Tre Universita Degli Studi. https://hdl.handle.net/20.500.14242/128338
Silleni A, Giordano G, Isaia R, Ort MH (2020) The magnitude of the 39.8 ka Campanian Ignimbrite eruption, Italy: method, uncertainties and errors. Front Earth Sci 8:1–22. https://doi.org/10.3389/feart.2020.543399
Silleni A, Giordano G, Ort M, Isaia R (2024) The transport and deposition of the 39.8 ka Campanian Ignimbrite large-scale pyroclastic density currents (Italy). Geol Soc Am Bull 136(11–12):4877–4895. https://doi.org/10.1130/B37500.1
Smith VC, Isaia R, Engwell SL, Albert PG (2016) Tephra dispersal during the Campanian Ignimbrite (Italy) eruption: implications for ultra-distal ash transport during the large caldera-forming eruption. Bull Volcanol 78:45. https://doi.org/10.1007/s00445-016-1037-0
Sparks RSJ, Wilson L, Hulme G (1978) Theoretical modeling of the generation, movement, and emplacement of pyroclastic flows by column collapse. J Geophys Res 83:1727–1739
Stock MJ, Humphreys MCS, Smith VC, Isaia R, Pyle DM (2016) Late-stage volatile saturation as a potential trigger for explosive volcanic eruptions. Nat Geosci 9:249–254. https://doi.org/10.1038/ngeo2639
Stock MJ, Humphreys MCS, Smith VC, Isaia R, Brooker RA, Pyle DM (2018) Tracking volatile behaviour in sub-volcanic plumbing systems using apatite and glass: insights into pre-eruptive processes at Campi Flegrei, Italy. J Pet 59:2463–2492. https://doi.org/10.1093/petrology/egy020
Tait S, Jaupart C, Vergniolle S (1989) Pressure, gas content and eruption periodicity of a shallow, crystallising magma chamber.

Earth Planet Sci Lett 92:107–123. https://doi.org/10.1016/0012-821x(89)90025-3

Tomlinson EL, Arienzo I, Wulf S, Smith VC, Carandente A, Civetta L, Hardiman M, Lane CS, Orsi G, Rosi M, Thirlwall MT, Muller W, Menzies MA (2012) Geochemistry of the Phlegraean Fields (Italy) proximal sources for major Mediterranean tephras: implications for the dispersal of Plinian and co-ignimbritic components of explosive eruptions. Geochim Cosmochim Acta 93:102–128. https://doi.org/10.1016/j.gca.2012.05.043

Trolese M, Cerminara M, Esposti Ongaro T, Giordano G (2019) The footprint of column collapse regimes on pyroclastic flow temperatures and plume heights. Nat Commun 10:2476. https://doi.org/10.1038/s41467-019-10337-3

Vitale S, Isaia R (2014) Fractures and faults in volcanic rocks (Campi Flegrei, southern Italy): insight into volcano-tectonic processes. Int J Earth Sci 103:801–819. https://doi.org/10.1007/s00531-013-0979-0

Wallace PJ (2001) Volcanic SO_2 emissions and the abundance and distribution of exsolved gas in magma bodies. J Volcanol Geotherm Res 108:85–106. https://doi.org/10.1016/S0377-0273(00)00279-1

Wallace PJ, Anderson AT Jr, Davis AM (1995) Quantification of pre-eruptive exsolved gas contents in silicic magmas. Nature 377:612–616

Webster JD, Raia F, Tappen C, De Vivo B (2003) Pre-eruptive geochemistry of the ignimbrite-forming magmas of the Campanian Volcanic Zone, southern Italy, determined from silicate melt inclusions. Mineral Petrol 79:99–125. https://doi.org/10.1007/s00710-003-0004-6

Wieser P, Iacovino K, Matthews S, Moore G, Allison CM (2022) VESIcal: 2. a critical approach to volatile solubility modeling using an open-source Python3 engine. Earth Space Sci. https://doi.org/10.1029/2021EA001932

Wieser P, Petrelli M, Lubbers J, Kent A, Till C (2021) Thermobar: a critical evaluation of mineral-melt thermobarometry and hygrometry in arc magmas using a new open-source Python 3 tool. Geol Soc Am Ann Mtg Abstract 203–5. https://doi.org/10.1130/abs/2021am-367080

Wilson CJ, Cooper GF, Chamberlain KJ, Barker SJ, Myers ML, Illsley-Kemp F, Farrell J (2021) No single model for supersized eruptions and their magma bodies. Nat Rev Earth Environ 2:610–627. https://doi.org/10.1038/s43017-021-00191-7

Zhang X, Ganguly J, Ito M (2010) Ca–Mg diffusion in diopside: tracer and chemical inter-diffusion coefficients. Contrib Mineral Petrol 159:175–186. https://doi.org/10.1007/s00410-009-0422-5

Zollo A, Maercklin N, Vassallo M, Dello Iacono D, Virieux J, Gasparini P (2008) Seismic reflections reveal a massive melt layer feeding Campi Flegrei caldera. Geophys Res Lett 35:L12306. https://doi.org/10.1029/2008GL034242